nature communications

Article

https://doi.org/10.1038/s41467-026-75811-1

# Anchoring mechanism-inspired discovery of a bacterial P450 gene conferring resistance to auxin herbicides

Received: 22 November 2025

Accepted: 13 July 2026

Published online: 25 July 2026

Check for updates

Yuanyuan Jiang[1,2,9], Junjie Zhang[3,9], Zhong Li[1], Lingyan Wang[4], Yuyu Guo[1], Yuxuan Li[1], Xisong Feng[1], Wen Gao[3], Yong Li[3], Zijia Li[5], Jieke Du[1], Guoqiang Zhang[1], Piqian Gong[1], Wenhan Fang[6], Xiang Gao[1], Mingyi Bai[4], Frank Hollmann[7], Mei Zhang[8], He Huang[5], Binju Wang[6], Sudong Mo[3] ✉, Huarong Li[3], Wei Peng[1] ✉ & Shengying Li[1,2] ✉

Herbicides in combination with genetically modified herbicide-resistant crops have revolutionized modern weed management, increased crop yields, and facilitated farming practices. However, rapid evolution of herbicide-resistant weeds necessitates new resistance traits to sustain control efficacy. Here, we introduce a terminal carboxyl anchoring mechanism-inspired approach for precise discovery of P450 herbicide resistance genes, by which a number of bacterial P450 peroxygenases are predicted and confirmed to degrade auxin herbicides. Upon enzyme engineering, the optimal mutant $P450_{BSβ}$-F46A can efficiently degrade diverse auxin herbicides and other carboxyl-containing herbicides. Mechanistic studies reveal that Compound I-mediated hydroxylation initiates the C–O bond cleavage, followed by aromatic ring hydroxylation, thus forming a unique two-step degradation pathway. Transgenic rice expressing *$P450_{BSβ}$-F46A-CPR* confers significant resistance to a recently commercialized auxin herbicide fluchloraminopyr. This work demonstrates the potential of the mechanism-driven strategy in directed discovery of broad-spectrum resistance genes for herbicide-resistant crop engineering.

Weeds are a major threat to crop production worldwide[1,2]. Auxin herbicides, which mimic the plant hormone auxins (e.g., indole-3-acetic acid, IAA), have been among the most successful herbicides used for weed control[3,4]. These synthetic compounds disrupt weed growth by triggering abnormal, prolonged auxin-mediated responses due to their higher metabolic stability[5–7]. The commercialization of 2,4-dichlorophenoxyacetic acid (2,4-D, **1**) in 1945 initiated continuing chemical diversification efforts that, driven by agricultural demands, have led to various auxin herbicide classes, such as 2-(2,4-dichlorophenoxy)propionic acid (2,4-DP, **2**), 2,4-dichlorophenoxybutyric acid (2,4-DB, **3**), 2-methyl-4-chlorophenoxyacetic acid (MCPA, **4**), 2-(2-methyl-4-chlorophenoxy)propionic acid (MCPP, **5**), 2-methyl-4-chlorophenoxybutyric acid (MCPB, **6**), and fluchloraminopyr (**7**)) with distinct weed spectra and selectivity profiles (Fig. 1a)[8,9]. However,

[1]State Key Laboratory of Microbial Technology, Shandong University, Qingdao, China. [2]Laboratory for Marine Biology and Biotechnology, Qingdao Marine Science and Technology Center, Qingdao, China. [3]Qingdao KingAgroot CropScience Co., Ltd., Qingdao, China. [4]The Key Laboratory of Plant Development and Environmental Adaptation Biology, School of Life Sciences, Shandong University, Qingdao, China. [5]School of Food Science and Pharmaceutical Engineering, State Key Laboratory of Microbial Technology, Nanjing Normal University, Nanjing, China. [6]College of Chemistry and Chemical Engineering, Xiamen University, Xiamen, China. [7]Department of Biotechnology, Delft University of Technology, Delft, The Netherlands. [8]Guangdong Provincial Key Laboratory of Applied Botany, South China Botanical Garden, Chinese Academy of Sciences, Guangzhou, China. [9]These authors contributed equally: Yuanyuan Jiang, Junjie Zhang. ✉e-mail: mosudong-qy@kingagroot.com; weipeng@sdu.edu.cn; lishengying@sdu.edu.cn

https://doi.org/10.1038/s41467-026-75811-1

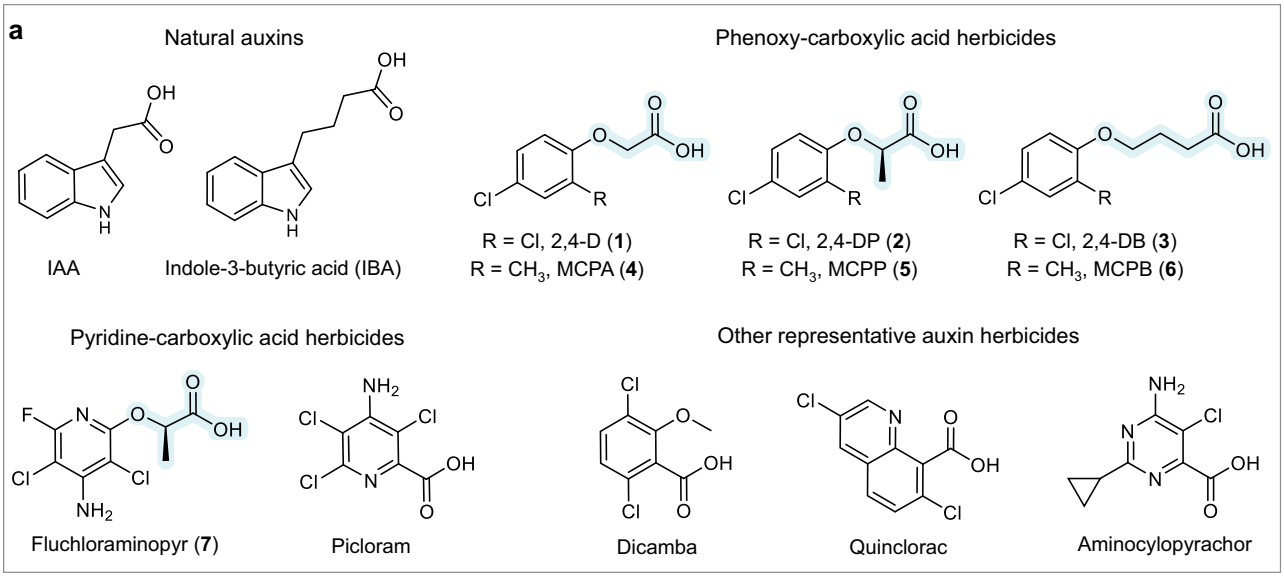


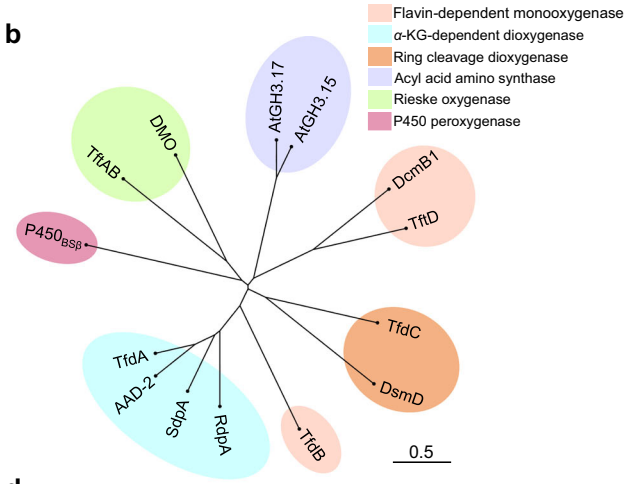


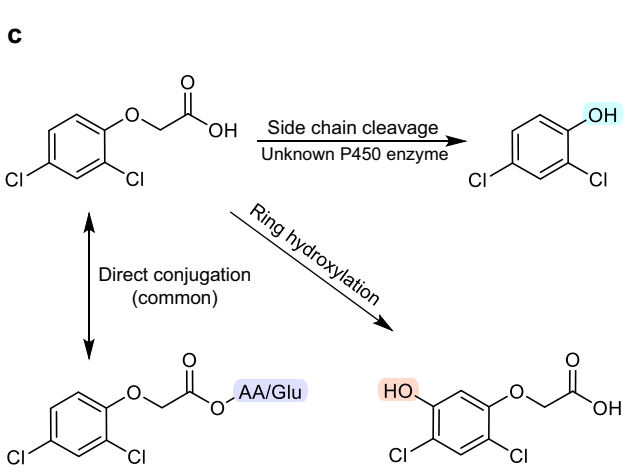


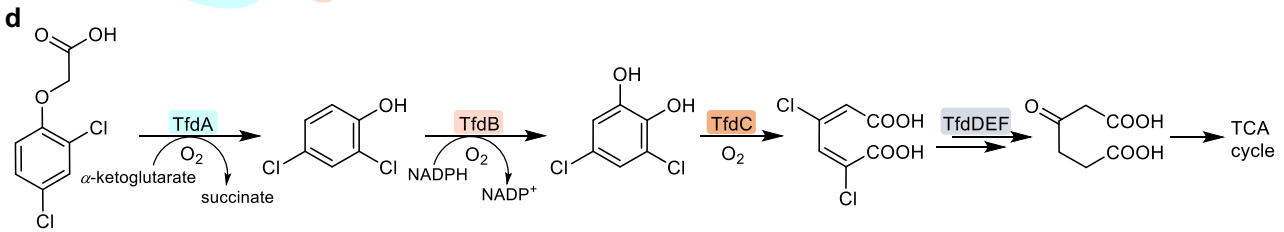


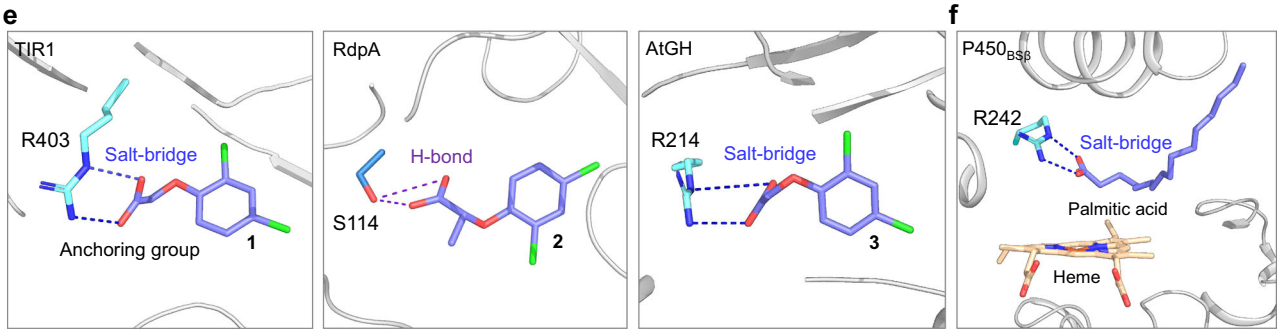


the massive use of auxin herbicides in agriculture has not only caused crop phytotoxicity, but also resulted in the evolution of resistant weeds[10–14].

Genetically modified crops with herbicide-resistant traits have been developed to mitigate these problems. Thus, combining a herbicide and its specific resistance trait is indispensable for modern crop breeding[10,11,15,16]. Of note, the discovery of new resistance traits heavily relies on the identification of enzymes involved in herbicide degradation pathways[6,17–19]. To date, these enzymes remain largely confined to natural herbicide-resistant plants and degrading microorganisms, whereas enzymes targeting auxin mimics typically display narrow substrate scope (Fig. 1b–d and Supplementary Table 2)[12,20–23]. This limitation significantly slows the discovery of novel resistance genes, especially for newly emerging herbicides. Thus, there is an urgent need

**Fig. 1 | Directed discovery of P450 peroxygenases for degrading auxin herbicides via a terminal carboxyl-anchoring mechanism. a** Structures of natural auxins and representative synthetic auxin herbicides belonging to different chemical classes. 2,4-D: 2,4-dichlorophenoxyacetic acid; MCPA: 2-methyl-4-chlorophenoxyacetic acid; 2,4-DP: 2-(2,4-dichlorophenoxy)propionic acid; MCPP: 2-(2-methyl-4-chlorophenoxy)propionic acid; 2,4-DB: 2,4-dichlorophenoxybutyric acid; MCPB: 2-methyl-4-chlorophenoxybutyric acid. **b** Phylogenetic analysis of representative known enzymes involved in the degradation of synthetic auxin herbicides and P450 peroxygenase studied in this work. **c** Metabolic pathways of **1** in higher plants. AA: amino acid; Glu: glucose. **d** A typical microbial degradation pathway of **1**. TCA cycle: tricarboxylic acid cycle. **e** The terminal carboxyl anchoring mechanisms of auxin receptor TIR1 ubiquitin ligase (PDB ID code: 2P1N) and auxin degrader proteins including aryloxyalkanoate dioxygenase RdpA (PDB ID code: 5BKB) and acyl acid amido synthetase AtGH3.15 (PDB ID code: 6E1Q). **f** The key interactions between the terminal carboxyl group of fatty acid substrate and the conserved arginine residue in the active site of the representative CYP152 peroxygenase $P450_{BS\beta}$ (PDB ID code: 1IZO).

for an effective approach to direct novel resistance gene discovery that targets new herbicides.

The recently approved pyridine-carboxylic acid herbicide **7** features a carboxyl side chain with an ether linkage, structurally resembling phenoxy-carboxylic acid herbicides (Fig. 1a). Regarding the reported action and degradation mechanisms of phenoxy-carboxylic acid herbicides (Fig. 1e)[6,21,24], crystallographic analyses have revealed that IAA and auxin analogs bind to the auxin receptor or degrader proteins via their terminal carboxyl group by forming either salt bridges with an arginine residue or hydrogen bonds with a serine residue. These structural insights indicate that the carboxylic side-chain of auxin herbicides acts as an anchoring group, thereby enabling binding to diverse target proteins and triggering the resistance-related metabolic reactions. Inspired by this substrate/ligand anchoring mechanism, we reasoned that it could guide the search for versatile degrading enzymes with a similar substrate-enzyme interaction mode to accelerate the discovery of effective resistance traits for **7** and other auxin herbicides.

Cytochrome P450 (CYP) enzymes are recognized as the most versatile biocatalysts in herbicide metabolisms[25,26]. Experiments with P450 inhibitors have demonstrated that some unknown P450 enzymes could degrade auxin herbicides in resistant weeds (Fig. 1c). However, identification of the specific plant P450 genes is difficult due to the lack of detailed genome information and/or sophisticated gene-editing tools[27]. Building on our extensive knowledge of P450 enzymes[28–36] and guided by a sense of "déjà vu" on the terminal carboxyl anchoring mechanism of bacterial CYP152 peroxygenases[37–44], which is required for both substrate binding and substrate-assisted catalysis (Fig. 1f, Supplementary Figs. 1 and 2), we sought to find CYP152-based auxin herbicide resistance genes and construct resistant crop plants by genetically incorporating the degradation pathway.

In this study, we harness the terminal carboxyl anchoring mechanism to precisely identify CYP152 peroxygenases with broad-spectrum auxin herbicide detoxification capability, and enhance the degradation activity by substrate access channel engineering. The degradation mechanism, featuring a unique Compound I-mediated C–O bond cleavage reaction, is elucidated by structural and substrate docking analyses, $^{18}O$ isotope tracing experiments, and QM/MM calculations. The expression of *$P450_{BS\beta}$-F46A-CPR* gene in rice confers significant resistance to **7**, suggesting that the integration of P450-based transgenic rice with auxin herbicides could serve as a sustainable solution for weed control.

## Results

### Anchoring mechanism-inspired discovery of P450 enzymes capable of degrading auxin herbicides

Inspired by the terminal carboxyl anchoring mechanism shared by auxin herbicide receptor and degrader proteins (Fig. 1e), we surmised that CYP152 peroxygenases might be capable of modifying auxin herbicides because this family of $H_2O_2$-dependent P450 enzymes adopt a similar substrate anchoring mechanism via the conserved guanidyl-carboxyl interaction (Fig. 1e, f and Supplementary Figs. 1 and 2)[40,41]. Pursuing this, we evaluated three representative CYP152 peroxygenases, including $OleT_{JE}$, $P450_{BS\beta}$ and $P450_{SP\alpha}$, which are known for their distinct fatty acid decarboxylation/hydroxylation preferences[40,41], to assess their degradation ability against a number of phenoxy-carboxylic acid herbicides with various side chains (**1**–**6**) and the recently approved nonselective pyridine-carboxylic acid herbicide **7**. Using the well-established AldO/glycerol-based in situ $H_2O_2$ releasing system[45], we found that both $OleT_{JE}$ and $P450_{BS\beta}$ catalyzed the C–O bond cleavage of **1**–**3, 4**–**6**, and **7**, giving rise to nonherbicidal 2,4-dichlorophenol (**8**), 2-methyl-4-chlorophenol (**12**), and 4-amino-3,5-dichloro-6-fluoropyridin-2-ol (**16**; Supplementary Figs. 3–5), respectively. Comparatively, these two P450 enzymes preferred to degrade **3** and **6**, with the highest substrate conversion ratios of 83% and 88%, respectively. By contrast, $P450_{SP\alpha}$ only exhibited a fairly low hydroxylation activity for **3** and **6**. Of note, the degradation product **8** underwent further aromatic hydroxylation to generate 3,5-dichlorocatechol (**9**), demonstrating a previously unreported two-step degradation pathway consecutively mediated by a single P450 enzyme.

### Substrate access channel engineering of $P450_{BS\beta}$ to enhance the degradation activity of auxin herbicides

$P450_{BS\beta}$ was selected for further enhancement of auxin herbicide degradation activity due to its superior activity and stability (Fig. 2a)[46]. As straight-chain fatty acids are the preferred substrates of wild-type $P450_{BS\beta}$, it features a narrow substrate access channel composed mainly of five phenylalanine residues (Phe46, Phe79, Phe173, Phe289, and Phe292; Fig. 2b)[37]. Given the sterically demanding nature of auxin herbicide substrates, we reasoned that widening the substrate access channel may increase the activity of $P450_{BS\beta}$ towards auxin herbicides. We therefore individually replaced the bulky phenylalanine residue with alanine[47,48], giving rise to five mutants including $P450_{BS\beta}$-F46A, $P450_{BS\beta}$-F79A, $P450_{BS\beta}$-F173A, $P450_{BS\beta}$-F289A, and $P450_{BS\beta}$-F292A. As expected, all these mutants displayed enhanced activities against all tested auxin herbicides (**1**–**7**; Fig. 2c–e, Supplementary Figs. 6 and 7, Supplementary Table 3), with $P450_{BS\beta}$-F46A demonstrating the highest conversion ratio.

Specifically, $P450_{BS\beta}$-F46A demonstrated a remarkable C–O bond cleavage activity towards **7**, achieving a conversion ratio of 86% (Fig. 2e, Supplementary Figs. 8 and 9). For **1** and **2**, $P450_{BS\beta}$-F46A significantly increased the marginal conversions of wild-type $P450_{BS\beta}$ to 11% and 29%, producing the nonherbicidal products **8** and **9**, respectively (Fig. 2d, Supplementary Figs. 10 and 11). The conversion of **3** was boosted to ~100% by this mutation. $P450_{BS\beta}$ and its mutants cleaved the ether bond of auxin herbicides, and further catalyzed the *ortho*-hydroxylation of **8** giving **9**, which could serve as a key intermediate for ring opening in a subsequent biodegradation pathway (Fig. 2d, Supplementary Figs. 12–15)[49]. Notably, **9** was the main end product of **3** when using $P450_{BS\beta}$-F46A and $P450_{BS\beta}$-F173A. By contrast, wild-type $P450_{BS\beta}$ produced **8** as the main product, accompanied by a small amount of **9** (Fig. 2d, Supplementary Fig. 12)[50]. In addition to the ether cleavage product, a minority of $\alpha$- and $\beta$-hydroxylation products of **3** were also observed, namely, 2,4-dichlorophenoxy-2*S*-hydroxybutyric acid (**10**) and 2,4-dichlorophenoxy-3*R*-hydroxybutyric acid (**11**), respectively (Fig. 2d, Supplementary Figs. 16–33, Supplementary Tables 4 and 5).

In comparison, **12** was consistently identified as the major product upon cleavage of the ether linkage of **4**–**6** (Fig. 2d, Supplementary

https://doi.org/10.1038/s41467-026-75811-1

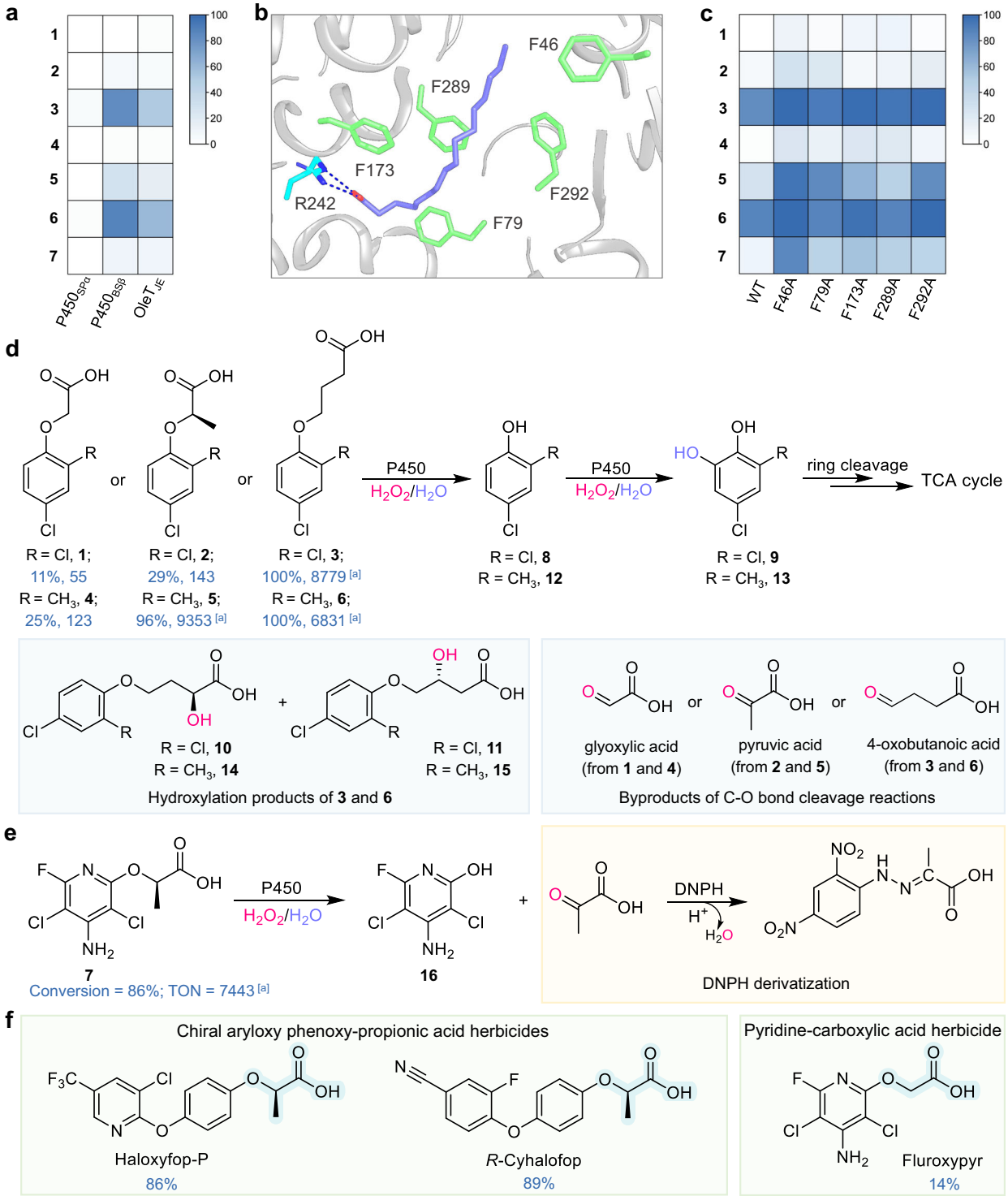


**Fig. 2 | CYP152 peroxygenase variants catalyze degradation of chemically diverse auxin herbicides. a** The activities of three representative CYP152 peroxygenases towards seven selected auxin herbicides. The intensity of blue colour indicates the differential substrate conversion ratios. **b** Five phenylalanine residues in the active site of $P450_{BSβ}$ subject to alanine scanning mutagenesis. **c** The activities of wild-type $P450_{BSβ}$ (WT) and its mutants towards **1**–**7**. **d** The CYP152 peroxygenase-mediated degradation pathway of phenoxy-carboxyl acid herbicides (**1**–**6**). The substrate conversion ratios (%) and TONs are shown below each individual substrate. **e** The CYP152 peroxygenase-mediated degradation pathway of **7** and DNPH-derivatization of its side-chain cleavage product. DNPH: 2,4-dinitrophenylhydrazine. **f** Degradation of other widely used herbicides containing a carboxyl anchoring group. Reaction conditions: 1 μM P450, 500 μM substrate, and the AldO/glycerol system (5 μM/10%) to generate $H_2O_2$ in situ at 30 °C for 6 h. [a] 10 mM substrate, 0.5 μM P450, and the AldO/glycerol system (5 μM/10%) to generate $H_2O_2$ in situ at 30 °C for 12 h. Source data for Fig. 2a, c are available in the Source Data file.

**Table 1 | Steady-state kinetic parameters and substrate dissociation constants of $P450_{BSβ}$ and $P450_{BSβ}$-F46A against representative auxin herbicides**

| Enzymes | Substrates | Kinetic parameters | | | Substrate dissociation constants ($K_D$/μM) |
|---|---|---|---|---|---|
| | | $k_{cat}$ ($min^{-1}$) | $K_m$ (μM) | $k_{cat}/K_m$ ($mM^{-1}$ $min^{-1}$) | |
| $P450_{BSβ}$ | **3** | 23 ± 2 | 1454 ± 170 | 15.8 | 2.93 ± 0.92 |
| | **5** | 10 ± 1 | 1092 ± 124 | 9.2 | 0.66 ± 0.08 |
| | **6** | 24 ± 2 | 1550 ± 260 | 15.4 | 0.68 ± 0.37 |
| | **7** | 11 ± 1 | 1416 ± 210 | 7.8 | NB |
| $P450_{BSβ}$-F46A | **3** | 37 ± 2 | 452 ± 59 | 81.9 | 0.71 ± 0.11 |
| | **5** | 31 ± 2 | 919 ± 96 | 33.7 | 0.24 ± 0.04 |
| | **6** | 31 ± 2 | 354 ± 70 | 87.6 | 0.42 ± 0.15 |
| | **7** | 17 ± 2 | 1385 ± 329 | 12.3 | 1.33 ± 0.43 |

All experiments were performed in triplicate. *NB* no binding.

Figs. 34–38). For **5**, wild-type $P450_{BSβ}$ gave a substrate conversion of 29%, while $P450_{BSβ}$-F46A significantly improved it to 96% and further oxidized **12** into 3-methyl-5-chlorocatechol (**13**; Fig. 2d, Supplementary Figs. 39–43, Supplementary Table 6). During the transformation of **6**, *α*- and *β*-hydroxylation reactions occurred again, resulting in minor products 2-methyl-4-cholorophenoxy-2*S*-hydroxybutyric acid (**14**) and 2-methyl-4-cholorophenoxy-3*R*-hydroxybutyric acid (**15**; Fig. 2d, Supplementary Figs. 44–61, Supplementary Tables 7–8). Of note, all $P450_{BSβ}$ mutants (except the wild-type enzyme) produced **13** when using **12** as a substrate (Supplementary Fig. 39). The $k_{cat}/K_m$ values further indicated that $P450_{BSβ}$-F46A exhibited higher catalytic efficiency compared to $P450_{BSβ}$ in catalyzing the reactions of four representative auxin herbicides, with a specific 4.7-fold increase for **6** (Table 1, Supplementary Figs. 62 and 63).

To directly illustrate how the F46A mutation alleviates steric hindrance and weakens unfavorable substrate–channel interactions, thereby enhancing substrate binding and reaction kinetics, we performed umbrella sampling simulations to map the dynamic entry and associated free-energy profiles of substrate **7** and intermediate **8** from bulk solvent into the active site (Supplementary Figs. 64–65 and Supplementary Movies 1–2). The simulations clearly show that, in the wild-type enzyme, π–π stacking between substrate **7** and F46 substantially retard substrate entry and imposes a pronounced steric barrier, resulting in a high free-energy barrier of ~30 kcal/mol. Notably, the position of this barrier coincides with the distance at which **7** engages in π–π interactions with F46 (21.3 Å). In contrast, F46A abolishes the π–π and steric constraints, markedly lowering the entry barrier (~13 kcal/mol at 19.6 Å) and enabling rapid substrate access to the active site. Umbrella sampling of intermediate **8** reveals a similar trend, corroborating the pivotal role of the F46A mutation in facilitating substrate ingress (Supplementary Fig. 65).

### Catalytic hydroxylation by $P450_{BSβ}$-F46A initiates C–O bond cleavage in auxin herbicides

To elucidate the intriguing mechanism by which $P450_{BSβ}$-F46A cleaves the C–O bond of **7** and **1**–**3** with varying side chains, we initially confirmed that **16** was a stable product, while **8** underwent further aromatic hydroxylation to produce **9** (Fig. 2d, e and Supplementary Figs. 9, 13, 15 and 66). To gain a deeper understanding of the substrate-enzyme interactions between $P450_{BSβ}$-F46A and auxin herbicides, we individually docked **7** and **1**–**3** into the active site of $P450_{BSβ}$-F46A (PDB ID code: 9IY1)[50] and refined the conformation of the enzyme-substrate complexes in the presence of $H_2O_2$ by MD simulations (Supplementary Fig. 67). We also validated the binding pose using combined QM/MM calculations (Fig. 3b)

The results demonstrate that, despite their distinct ring substituent structures and varying side chains, the four synthetic auxin analogs display similar binding modes within $P450_{BSβ}$-F46A (Fig. 3, Supplementary Fig. 68). These herbicides unanimously form salt bridges with the conserved R242 residue via their terminal carboxyl group, thereby anchoring the molecules at the bottom of the substrate binding pocket. For the enzyme-**7**-$H_2O_2$ complex, the proximal hydrogen atom of $H_2O_2$ forms a hydrogen bond with the oxygen atom of the substrate carboxyl group, stabilizing its coordination to the heme-iron atom (Fig. 3b). Additionally, the halogen atoms in substrates participate in halogen-π interactions with the neighboring phenylalanine residues (Fig. 3b–d, Supplementary Fig. 68). As a common result, the $C_α$–H of these substrates is positioned above the heme-iron.

To ascertain the catalytic significance of the carboxyl group, we examined the activity of $P450_{BSβ}$-F46A towards two synthetic auxin herbicide analogs lacking the carboxyl group (Supplementary Fig. 69). Neither 2,4-dichlorophenoxybutanol (**17**) nor 2,4-dichlorophenoxybutane (**18**) underwent any transformation, indicating that the substrate carboxyl group is essential for catalysis (Supplementary Figs. 70–77, Supplementary Tables 9 and 10). Site-directed mutagenesis analysis revealed the indispensable role of the conserved arginine residue (R242) in facilitating the catalytic process (Supplementary Figs. 78–89), which is crucial for substrate anchoring, as the binding affinities of auxin herbicides to $P450_{BSβ}$-F46A-R242A were markedly decreased by the R-to-A mutation (Supplementary Table 14).

Next, our MD simulation results revealed a fairly stable hydrogen bond network within the enzyme-**7**-$H_2O_2$ system, especially the one formed between the substrate carboxyl group and the proximal H1 of $H_2O_2$ (Fig. 3b, Supplementary Figs. 67, 90 and 91). Similar to normal catalysis of CYP152 peroxygenases towards fatty acids[45], the ether cleavage reaction likely also proceeds via a heterolytic O–O cleavage to form the reactive species Compound I (Cpd I; Fig. 4a, Supplementary Fig. 91). Our spin-state analysis indicates that the initial step involves proton transfer (PT) to form an Fe(III)–$OOH^-$ intermediate, followed by proton back-transfer–driven O–O heterolysis. Consistently, the spin density on the distal $OH^-$ remains close to zero both before and after the reaction, supporting a heterolytic cleavage pathway (Supplementary Table 15). Furthermore, QM/MM calculations indicate that Cpd I–mediated hydrogen abstraction from the C*α* position proceeds with an energy barrier of 21.1 kcal/mol (Fig. 4a, Supplementary Figs. 92 and 93), generating Cpd II and a substrate-centered radical intermediate. Then, we performed kinetic isotope effect (KIE) experiments to target the hydrogen-abstraction step using the synthetic C*α*-deuterated substrate *d*-**7**, yielding a KIE value of 3.0 (Supplementary Figs. 94–99), which indicates that this hydrogen-abstraction step is the rate-limiting step during catalysis[51,52]. The subsequent OH-rebound requires a lower barrier of 7.2 kcal/mol and is strongly exothermic, leading to formation of the hydroxylated intermediate. (Fig. 4a, Supplementary Fig. 93). Further hybrid cluster-continuum (HCC) model calculations shows that the intermediate can undergo spontaneous decomposition in aqueous solution (Fig. 4b), where the water-mediated PT from OH to O atom facilitates spontaneous C–O bond cleavage with a small energy barrier of 10.5 kcal/mol, leading to the formation of **16** and pyruvic acid (Fig. 4b, Supplementary Fig. 100). Supporting this, the formation of pyruvic acid was experimentally detected (Fig. 2e, Supplementary Figs. 101–105).

The reaction mechanism of **1**–**3** parallels that of **7** (Fig. 4c, Supplementary Figs. 106–115). Substrates **1** and **2** undergo a specific $C_α$-hydroxylation (Supplementary Figs. 106–109), whereas substrate **3** is predominantly oxidized at the $C_γ$ position (Fig. 4c, Supplementary Figs. 110 and 111). In the QM/MM-predicted mechanism and energetics for the Cpd I-mediated oxidation of **3** (Fig. 4c, Supplementary Fig. 112), we observed that the most favorable reaction pathway involves the H-abstraction from the $C_γ$–H bond via $TS3_{[3]γ}$, which requires a relatively lower activation barrier comparing to the competing $C_α$–H (via

https://doi.org/10.1038/s41467-026-75811-1

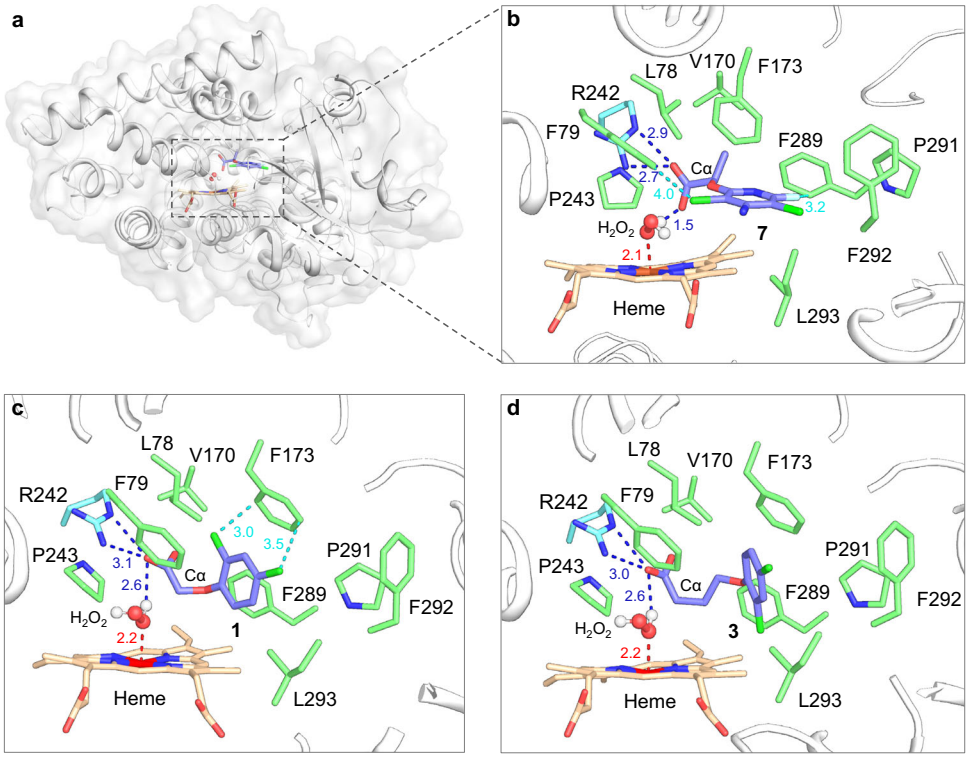


**Fig. 3 | Structural analysis of P450$_{BSβ}$-F46A with docked auxin herbicides reveals a conserved substrate anchoring mode via guanidyl-carboxyl interaction. a** Overall structure of P450$_{BSβ}$-F46A (PDB ID code: 9IY1) with docked **7** in the presence of $H_2O_2$. The heme group, $H_2O_2$, and **7** are shown as sticks. **b**–**d** QM/MM optimized P450$_{BSβ}$-F46A-substrate complex with the existence of $H_2O_2$. The complex structures of P450$_{BSβ}$-F46A are docked with substrate **7** (**b**), **1** (**c**), and **3** (**d**) in the presence of $H_2O_2$ in the active site. The key amino acids involved in the enzyme-substrate interactions are labeled and depicted as sticks, including R242 participating in polar interactions, F79, F173 and F289 engaging in halogen-π interactions, along with hydrophobic amino acids that facilitate non-specific hydrophobic interactions (within a 4.0 Å distance range). The carbon atoms of all substrates are depicted in purple, chlorine atoms in green, fluorine atoms in light-blue, and oxygen atoms in red. Blue dashed lines represent hydrogen bonds, cyan dashed lines indicate halogen-π bonds, and red dashed lines illustrate the Fe–O distance in angstroms.

TS3$_{[3]α}$) and $C_β$–H (via TS3$_{[3]β}$) abstraction routes (Fig. 4c). The $C_γ$–H oxidation directly generates a hydroxylated intermediate (Fig. 4c), and water-mediated PT from O1 to O2 drives spontaneous C–O bond cleavage, affording **8** and 4-oxobutanoic acid (Supplementary Fig. 113). Further, our calculations show that the hydroxyl oxygen in the stable hydroxylated products (**10** or **11** in Fig. 4c) should originate from $H_2O_2$, whereas the hydroxyl oxygen atoms in the C–O cleavage products **8** and **16** should not derive from either hydrogen peroxide or water, but rather from the substrate itself. These findings align with $H_2{}^{18}O_2$/$H_2{}^{18}O$ tracing experiments (Supplementary Figs. 116–121). The side chain cleavage products glyoxylic acid, pyruvic acid, and 4-oxobutyric acid were identified from the enzymatic reactions of **1**/**4**, **2**/**5**, and **3**/**6**, respectively (Fig. 2d, Supplementary Figs. 122–139).

## Catalytic versatility of P450$_{BSβ}$-F46A in degrading carboxylate-containing herbicides

To assess the catalytic versatility of the optimal mutant P450$_{BSβ}$-F46A in mediating C–O bond cleavage across structurally distinct carboxylate-containing herbicides, we selected the widely used chiral aryloxy phenoxy-propionic acid herbicides, including haloxyfop-P and *R*-cyhalofop (ACCase inhibitors), as substrates (Fig. 2f)[53,54]. Both herbicides underwent selective degradation to carboxyl-free metabolites by P450$_{BSβ}$-F46A and even wild-type P450$_{BSβ}$ (Fig. 2f, Supplementary Figs. 140–148, Supplementary Table 11), confirming the broad-spectrum degradation capacity of this P450 peroxygenase.

To further test the bioremediation potential of P450$_{BSβ}$-F46A in auxin herbicide degradation and elucidate catalytic disparities, we performed comparative analyses of the turnover numbers (TONs) and dissociation constants ($K_D$) for different substrates (Fig. 2d, e, Table 1 and Supplementary Tables 3, 12–14). Specifically, P450$_{BSβ}$-F46A exhibited the highest TON with **5** (TON = 9353), which surpassed that of **4** by a significant margin of 76 times (TON = 123). Consistently, substrate titration experiments showed that **5** bound more tightly to this P450 enzyme than **4**, as evidenced by their $K_D$ values of 0.24 μM and 0.41 μM, respectively (Supplementary Figs. 149 and 150). P450$_{BSβ}$-F46A demonstrated remarkable catalytic activities towards **3**, **6** and **7**, giving maximum TONs of 8779, 6831 and 7443, respectively (Fig. 2d, e and Supplementary Table 13). It is worth noting that among the tested P450 peroxygenases, the preference of **3** over **2** and **1** was revealed as a common trend. The $K_D$ values emphasized that propionic acid herbicides such as **2** and **5** (with the same $K_D$ values of 0.24 μM) exhibited stronger binding affinity compared to butyric acid auxin herbicides (e.g., 0.71 μM of **3** and 0.42 μM of **6**) and acetic acid auxin herbicides (e.g., 0.64 μM of **1** and 0.41 μM of **4**). Our calculations suggest that the shift in substrate preference might be attributed to the differences in C–H bond dissociation energies and the distances between O1 of Cpd I and the hydrogen atom of the substrate to be abstracted (Supplementary Figs. 151 and 152).

Intriguingly, despite **2** and **5** differing only by a single substituent on the benzene ring, the degradation activity of the P450 peroxygenases against **5** with a 2-methyl substituent (TON = 9353) was much higher than that towards **2** with a 2-Cl substituent (TON = 353; Supplementary Table 12). Since these two compounds showed an identical $K_D$ value of 0.24 μM, we reasoned that the significant activity difference likely arises from the requirement for P450$_{BSβ}$-F46A to overcome a markedly higher energy barrier when attacking the $C_α$–H of **2** compared to **5** (Supplementary Figs. 109, 153, and 154). These results suggest that electronic and steric properties of benzene ring substituents

https://doi.org/10.1038/s41467-026-75811-1

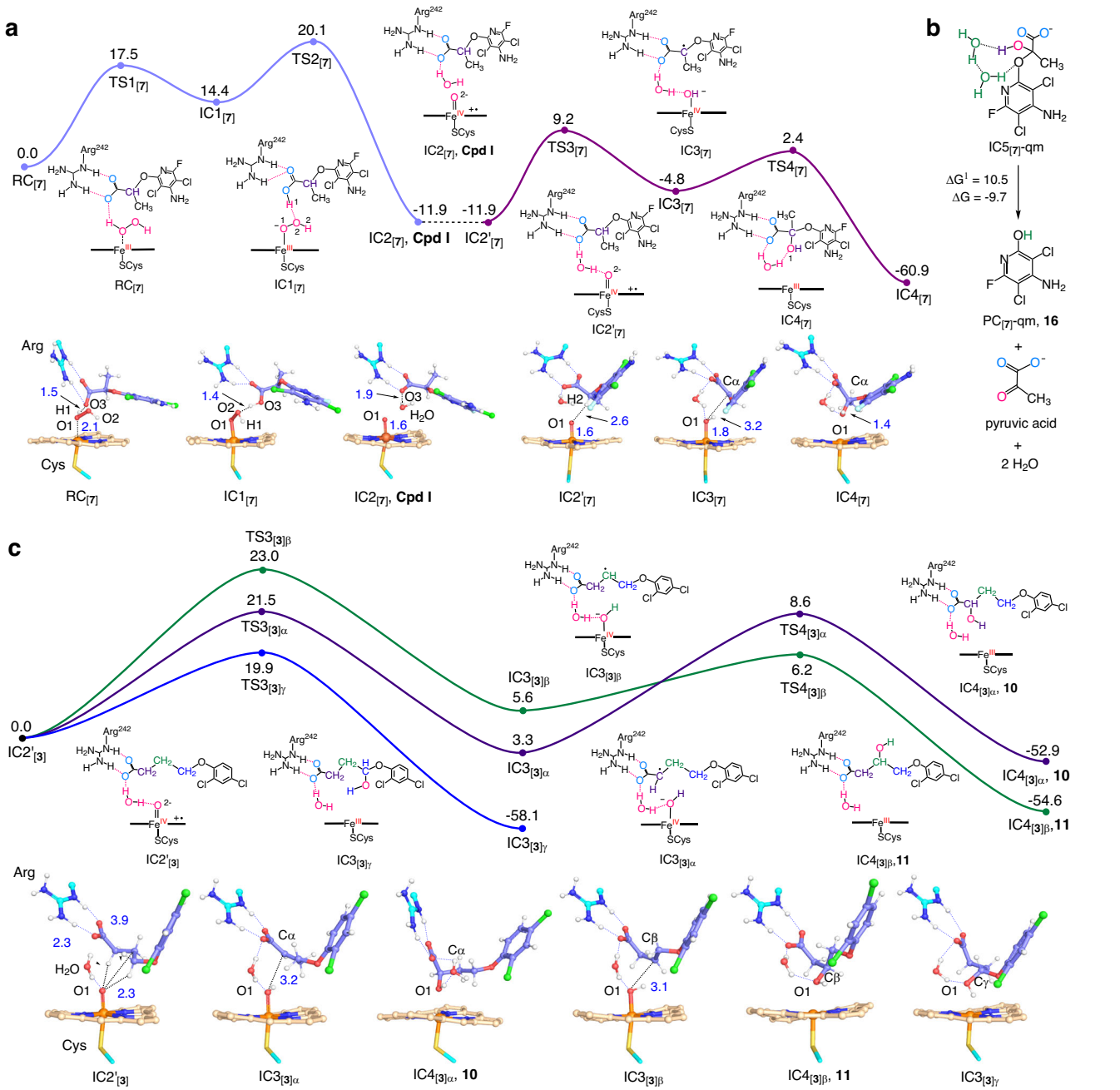


**Fig. 4 | Mechanism of the C–O bond cleavage of auxin herbicides catalyzed by P450$_{BSβ}$-F46A. a** QM(UB3LYP-D3/B2)/MM calculated mechanism (with energies in kcal/mol) for the formation of Cpd I by P450$_{BSβ}$-F46A in the presence of substrate **7** (left, light-blue) and Cpd I-mediated hydroxylation of **7** (right, purple). The key distances are given in angstrom (Å), along with the QM/MM optimized structures of key species involved in the reactions. **b** QM(BMK/6−311 + + G(d,p)) calculated energy barrier (in kcal/mol) for the water-mediated proton transfer and C–O cleavage of the hydroxylated intermediate of **7** to generate product **16**. **c** QM(UB3LYP-D3/B2)/MM calculated energy profile (kcal/mol) for Cpd I-mediated hydroxylation of **3**.

synergistically modulate the catalytic efficiency of P450 peroxygenases towards auxin herbicides.

## Transgenic rice expressing *P450$_{BSβ}$-F46A-CPR* confers resistance to the recently commercialized auxin herbicide fluchloraminopyr

Motivated by the successful combination and global adoption of nonselective herbicide glyphosate with glyphosate-resistant genetically modified crops[55], we explored the effects of expressing *P450$_{BSβ}$-F46A* in rice (Jingeng 818, an elite variety)[56] as a potential resistance gene against **7**, a recently commercialized nonselective auxin herbicide. In consideration of the limited availability of $H_2O_2$ cofactor inside plant cells, we fused P450$_{BSβ}$-F46A with a bacterial cytochrome P450 reductase (CPR) domain derived from P450 BM3[57,58] in order to generate hydrogen peroxide in situ by decoupling the NADPH-derived electrons to reduce dioxygen (Fig. 5a, Supplementary Figs. 155–157)[59]. The recombinant *P450$_{BSβ}$-F46A-CPR* gene was codon optimized and a chloroplast localization signal peptide from rice[60] was fused to its *N*-terminus. Expression of this fusion construct in transgenic rice was facilitated by the ubiquitin (UBI) promoter (Fig. 5a). Western blot analysis indicated the successful expression of P450$_{BSβ}$-F46A-CPR in transgenic rice cells (Fig. 5b). Subcellular localization experiments definitively showed that the specific P450 proteins, fused with a *C*-terminal

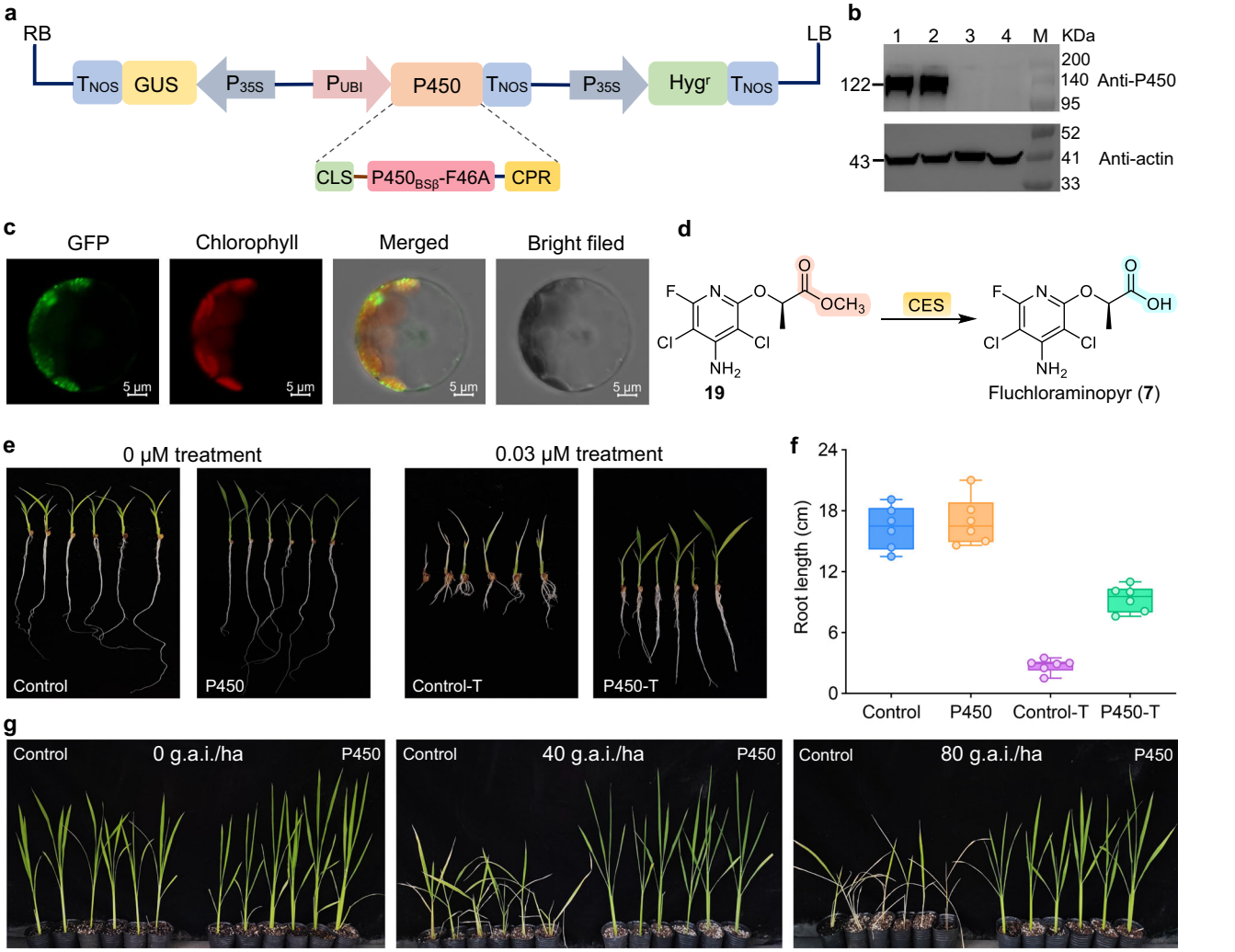


**Fig. 5 | Rice plants expressing *P450$_{BSβ}$-F46A-CPR* gene confer resistance to the nonselective auxin herbicide fluchloraminopyr. a** Schematic representation of the P450 gene construct. The pCambia1301 vector for expression of P450$_{BSβ}$-F46A-CPR in rice plants. Hyg$^r$ hygromycin resistance gene, GUS glucuronidase gene, $P_{35S}$ 35S promoter of *cauliflower mosaic virus*, $T_{NOS}$ terminator sequence of the nopaline synthase gene, LB left border, RB right border. **b** Western blot analysis of P450$_{BSβ}$-F46A-CPR expression in rice. Expression verification of P450$_{BSβ}$-F46A-CPR was conducted using anti-FLAG antibody (*top*). Lanes 1 and 2, independent transgenic plants; lanes 3 and 4, wild-type plants; M, protein marker. Actin was used as an internal control (*bottom*). Source data are provided in the Source Data file. **c** Subcellular location of P450$_{BSβ}$-F46A-CPR in rice. All experiments were independently repeated at least two times with similar results, and representative results are shown in Fig. 5b, c. **d** Pro-herbicide **19** undergoes hydrolysis into its active form **7**, via bioactivation by plant carboxylesterases (CES). **e** Phenotype of rice with and without the *P450$_{BSβ}$-F46A-CPR* transgene growing on MS medium containing 0.03 μM **19** for 21 days after germination. **f** Quantification of the root length of rice treated as (**e**). Data are shown as box-and-whisker plots with individual biological replicates overlaid ($n = 6$). Boxes span the 25th to 75th percentiles, with the center line indicating the median; whiskers extend to the minimum and maximum values. Individual dots represent biologically independent replicates. Source data are provided in the Source Data file. **g** Rice plants with and without the *P450$_{BSβ}$-F46A-CPR* transgene growing in soil were sprayed with different concentrations of **19**. Plant growth situations were recorded after 22 days.

GFP reporter[61], were localized within the chloroplasts as expected (Fig. 5c).

We subsequently investigated the resistance to **7** of the plants expressing *P450$_{BSβ}$-F46A-CPR*. This auxin herbicide is typically applied as a hydrophobic ester form (pro-herbicide: fluchloraminopyr-methyl, **19**; Fig. 5d) in the field to enhance its leaf permeability[62]. Once infiltrating plant tissues, **19** undergoes rapid hydrolysis catalyzed by abundant plant carboxylesterases, effectively activating the herbicide and releasing the toxic carboxylic acid form into the plant cells. Thus, we selected **19** for resistance testing in transgenic rice. Initially, both the wild-type and *P450$_{BSβ}$-F46A-CPR* transgene-expressing rice lines were cultivated in a medium containing 0.03 μM (critical concentration) of **19** (Supplementary Fig. 158). The growth of wild-type plants was strongly inhibited by **19**. By contrast, the transgenic rice exhibited significantly less growth impairment by **19**, as evidenced by their elongated roots (Fig. 5e, f). Next, a spray assay was performed using T1 transgenic rice plants, exposed to **19** at the concentrations of 40 and 80 g.a.i./ha. Under these conditions, no notable growth defects were observed in the transgenic plants. In contrast, the control wild-type plants displayed a strong growth inhibitory phenotype when treated with **19** (Fig. 5g). These findings confirmed that the genetically modified rice with integrated *P450$_{BSβ}$-F46A-CPR* gene confers substantial resistance to **7**, offering promising prospects for the cultivation of herbicide-resistant crops in the future.

## Discussion

In this study, we introduce an innovative mechanism-driven approach for the precise discovery of P450 peroxygenases as an effective resistance trait capable of detoxifying auxin herbicides, based on the common feature of terminal carboxyl anchoring mechanisms. The

optimal mutant P450$_{BSβ}$-F46A demonstrates broad applicability in cleaving C–O bonds of carboxyl-containing herbicides, including eight auxin herbicides and two chiral aryloxy phenoxy-propionic acid herbicides (Fig. 2, Supplementary Fig. 159). Compared to known auxin herbicide-degrading enzymes[6,21,49,63], this engineered P450 enzyme displays the widest substrate scope reported so far (Supplementary Table 2). Moreover, it simplifies the established environmental degradation pathways of **1** (Fig. 1d) by facilitating sequential C–O bond cleavage and aromatic ring hydroxylation reactions[49,64], ultimately yielding **9** as a ring-scission substrate for downstream mineralization pathways[65]. To the best of our knowledge, no prior study has reported a consecutive two-step degradation reaction of auxin herbicides catalyzed by a single enzyme.

All oxygenases reported to be involved in herbicide degradation operate through $O_2$-activation pathways[49,66]. Our discovery of a $H_2O_2$-dependent oxygenase expands the enzymatic diversity in this bioremediation process, revealing an example of convergent evolution where functionally analogous systems have independently evolved to address similar ecological challenges. Our mechanistic analysis of C–O bond cleavage initiated by P450$_{BSβ}$-F46A-catalyzed hydroxylation provides valuable insights into the molecular basis of unknown P450-mediated herbicide resistance in resistant weeds[27]. This work further advances our understanding of the catalytic versatility of CYP152 peroxygenase family by expanding its substrate and reaction scope. Unlike the conventional hydroxylation reaction of the aliphatic carboxylic acid by P450$_{BSβ}$ through a typical substrate $C_β$–H abstraction[37,67], the C–O bond cleavage reaction distinctly targets a hydrogen atom from the C–H bond adjacent to the oxygen atom of aromatic ether. This finding underscores the catalytic competence of CYP152 peroxygenases, emphasizing their potential as an enzyme resource for fostering catalytic multifunctionality and engineering new-to-nature activities[35,68].

In contrast to plant P450 monooxygenases, which display unpredictable substrate scopes and catalytic behaviors, thus leading to uncontrollable impacts on plant metabolisms[26], bacterial P450 peroxygenases exhibit higher substrate specificity and hence resolve the ambiguity associated with P450 functions in plant xenobiotic pathways. This specificity arises from their unique reliance on the carboxyl group of substrates for acid-base catalysis[42]. Like other auxin herbicide-degrading enzymes, P450$_{BSβ}$-F46A can also convert natural auxins (e.g., IAA) into hydroxylated derivatives (Supplementary Figs. 160 and 161) in a manner similar to the classical hydroxylation by plant metabolic pathways[6,69]. Nonetheless, this process does not impair plant growth, as cells maintain auxin levels primarily through de novo synthesis, a key regulatory mechanism that counteracts external hormone fluctuations[70]. The successful integration and expression of this recombinant P450 gene in rice demonstrated its ability to confer resistance to the target auxin herbicide without compromising the overall growth of the transgenic crops (Fig. 5g). Therefore, this discovery holds immense significance as it paves the way for developing genetically modified crops resistant to nonselective auxin herbicides (e.g., **7**), which could significantly boost agricultural productivity and sustainability when fully developed. Of note, P450$_{BSβ}$-F46A exhibits high TONs (up to 9353) for various auxin herbicides (Fig. 2d–f). This characteristic suggests its great potential as a versatile herbicide resistance gene for developing more sustainable crop varieties with broad-spectrum herbicide resistance, thus addressing the future challenges of herbicide-resistant weeds. Importantly, this enzyme could also facilitate bioremediation of environmental aromatic herbicide pollutants by generating catechol intermediates (Fig. 2d), which are essential for aromatic ring opening for the following complete mineralization[71]. Thus, this P450 enzyme holds considerable potential for removing residual herbicides from diverse ecosystems.

In summary, we have developed an anchoring mechanism-based approach for directed discovery of broad-spectrum P450 auxin herbicide resistance genes. The expression of *P450$_{BSβ}$-F46A-CPR* gene in rice conferring auxin herbicide resistance underscores the effectiveness of this approach and expands the molecular toolkit for sustainable crop defense. This combination of herbicide and resistance trait provides an effective tool to combat invasive weeds and mitigate resistance evolution. This work highlights P450 enzymes as a largely untapped source of herbicide resistance traits, owing to their evolutionary adaptability and catalytic versatility[32,72,73]. While the present research centers on monocot crops and the use of chiral propanoic acid herbicides, we envision that broader agricultural applications would be possible based on integrated technological approaches. Combining artificial intelligence-driven protein engineering with omics-guided genome-wide screening will enable smarter development of microbial and plant-derived P450 variants tailored for precision agriculture[74–76]. This work provides a paradigm for studying underexplored agronomically relevant resistance gene families, thereby accelerating the global shift toward sustainable agriculture.

## Methods

### Materials

All antibiotics and chemicals were purchased from Solarbio (Beijing, China), Sigma-Aldrich (St. Louis, MO, USA), Dr. Ehrenstorfer (Ausberg, Germany), TCI (Shanghai, China), Macklin (Shanghai, China), Aladdin Biochemical Technology (Shanghai, China), AnaStandard (Yangzhou, China), Baisai Biotechnology (Qingdao, China) or provided by King-Agroot (Qingdao, China), unless otherwise specified. Purification of DNA fragments was performed using the MonPureTM Gel & PCR Clean Kit from Baisai Biotechnology (Qingdao, China). Ni-NTA resin used for protein purification was acquired from Sangon Biotech (Shanghai, China). PD-10 desalting columns were purchased from GE Healthcare (Piscataway, NJ, USA). Millipore Amicon Ultra centrifugal filters were bought from Millipore (Billerica, MA, USA). The 10× QuickRunTM Fast Running Buffer and FlexiRunTM premixed gel solution for SDS-PAGE analysis were supplied by MDBio (Xinbei, China).

### Bioinformatics analysis

A neighbor-joining phylogenetic tree was constructed for P450$_{BSβ}$ (CYP152A1) and 13 known representative enzyme sequences involved in the degradation of synthetic auxin herbicides. Sequence alignment was performed using the ClustalW algorithm, and the phylogenetic tree was generated via the neighbor-joining method with 1000 bootstrap replicates. The resulting tree was visualized, annotated, and exported using the ITOL online tool (https://itol.embl.de/).

### Molecular cloning and protein purification

The constructs of single mutants including P450$_{BSβ}$-F46A, P450$_{BSβ}$-F79A, P450$_{BSβ}$-F173A, P450$_{BSβ}$-F289A and P450$_{BSβ}$-F292A, and double mutants including P450$_{BSβ}$-F46A-R242A, P450$_{BSβ}$-F46A-R242E, P450$_{BSβ}$-F46A-R242S and P450$_{BSβ}$-F46A-R242K were built by site-directed mutagenesis via overlap extension PCR using P450$_{BSβ}$ or P450$_{BSβ}$-F46A encoding genes as templates. The sequences of primers used in this study are listed in Supplementary Table 1. All cloned sequences were confirmed by DNA sequencing at Sangon Biotech (Shanghai, China), and then used to transform *E. coli* BL21 (DE3) for protein expression. The plasmids pET28b-*oleT$_{JE}$*, pET28b-*bsβ*, pET28b-*spα* and pET28b-*aldo* were available in our laboratory[45], which were generated by cloning the corresponding genes into pET28b between the *Nde*I and *Xho*I restriction sites.

The *E. coli* BL21 (DE3) cells carrying a certain recombinant expression vector were grown at 37 °C for 12 h with shaking at 220 rpm and then used as seed cultures to inoculate (1:50 ratio) a modified Terrific Broth medium containing a rare salt solution1. Cells were grown at 37 °C for 3–4 h until the optical density at 600 nm ($OD_{600}$) reached 0.8–1.0, to which isopropyl *β*-D-1-thiogalactopyranoside

(IPTG) was added to a final concentration of 0.2 mM. For P450 expression, 1 mM δ-aminolevulinic acid (5-ALA) and 1 mM thiamine were supplemented. Afterwards, the cultivation continued for another 24 h at 18 °C. The cells were harvested (6000 × *g*, 4 °C, 10 min) and stored at -80 °C for later use. Purification of $His_6$-tagged $OleT_{JE}$, AldO, and $P450_{BSβ}$ was performed as follows. Briefly, cell pellets were resuspended in lysis buffer (50 mM $NaH_2PO_4$, 300 mM NaCl, 10 mM imidazole, 10% glycerol, pH 8.0) and lysed using a high-pressure homogenizer (ATS, Shanghai, China) at 4 °C. The lysate was clarified by centrifugation (10,000 × *g*, 60 min, 4 °C). The supernatant was incubated with Ni–NTA agarose at 4 °C for 1 h with gentle mixing and then loaded onto a gravity-flow column. After washing with washing buffer (50 mM $NaH_2PO_4$, 300 mM NaCl, 20 mM imidazole, 10% glycerol, pH 8.0), the bound proteins were eluted with elution buffer (50 mM $NaH_2PO_4$, 300 mM NaCl, 250 mM imidazole, 10% glycerol, pH 8.0). The eluted proteins were concentrated using an Amicon Ultra centrifugal filter (30 kDa cutoff, Millipore) and buffer-exchanged into storage buffer (50 mM $NaH_2PO_4$, 10% glycerol, pH 7.4) using a PD-10 desalting column. Purified proteins were flash-frozen in liquid nitrogen and stored at −80 °C until use. For $OleT_{JE}$, the storage buffer additionally contained 500 mM NaCl. For AldO, all purification steps were performed using glycerol-free buffers.

### Enzyme concentration determination

Analysis of the UV-visible spectroscopic properties of $OleT_{JE}$, $P450_{SPα}$, and $P450_{BSβ}$ and their mutants was carried out[77]. For preparation of the dithionite-reduced ferrous-CO complex of each enzyme, the purified ferric enzymes were diluted in Desalting buffer (pH 7.4, 50 mM $NaH_2PO_4$, 10% glycerol) and subjected to slow CO bubbling for 40–50 s for initial scan at 350–600 nm to record the spectrum of the resting-state CO-bound proteins, and then followed by sufficient reduction of the protein by sodium dithionate to obtain the CO-bound reduced difference spectrum. The P450 protein concentrations were calculated based on their reduced CO-bound difference spectra[78] using the reduced differential extinction coefficient $\varepsilon_{450-490}$ of 91,000 $M^{-1}$ $cm^{-1}$. The concentration of AldO[79] was determined at 452 nm with the reported extinction coefficient of 12,500 $M^{-1}$ $cm^{-1}$.

### In vitro enzymatic assays

Since P450 $OleT_{JE}$ was characterized as a moderate halophilic protein requiring a salt solution to maintain its stability and activity[80], all the $OleT_{JE}$ reactions were carried out in a buffer containing 500 mM NaCl. A typical assay containing 1 μM $OleT_{JE}$, 500 μM substrate, and 5 μM AldO (optional) and 5% EtOH as co-solvent in 200 μL reaction buffer (pH 7.4, 50 mM $NaH_2PO_4$, 500 mM NaCl, 10% glycerol) was carried out at 30 °C for 6 h. A typical assay for $P450_{BSβ}$ and its mutants containing 1 μM P450, 500 μM substrate (**1**-**7**), 5 μM AldO, and 5% EtOH as co-solvent in 200 μL reaction buffer (pH 7.4, 50 mM $NaH_2PO_4$, 10% glycerol) was carried out at 30 °C for 6 h. The reactions were quenched by adding 200 μL methanol to precipitate proteins, vortexing for 5 min, and centrifuging at 14,000 × *g* for 10 min. Subsequently, the supernatants were taken and directly used for HPLC or LC-MS analysis; detailed analytical methods are described in Supplementary Method 1. As a negative control, the enzyme reactions were performed in the absence of P450 enzyme or AldO, neither of which showed catalytic activity toward the tested substrates. The substrate peak areas for the negative control reactions represented the total substrate amount. The conversion ratios were calculated based on the peak areas of enzymatic substrates versus authentic control standards, as analyzed by HPLC. All measurements were performed in triplicate. The preparation and characterization of the new reaction products are described in Supplementary Methods 2 and 3.

**The $^{18}O$-tracing experiments using $H_2{}^{18}O_2$.** The 200 μL reaction containing 1 μM $P450_{BSβ}$-F46A, 500 μM **3** or **7**, and 500 μM $H_2{}^{18}O_2$ (or $H_2O_2$ as control), and 5% EtOH as co-solvent was carried out at 30 °C for 6 h.

**The $^{18}O$-tracing experiments using $H_2{}^{18}O$.** The 200 μL reaction containing 1 μM $P450_{BSβ}$-F46A, 500 μM **3** or **7**, and 500 μM $H_2O_2$, and 5% EtOH as co-solvent was carried out at 30 °C for 6 h in $H_2{}^{18}O$ buffer.

**TON determination.** The reaction mixture contained certain reaction buffer, 1 μM P450 ($P450_{BSβ}$, $P450_{BSβ}$-F46A, $P450_{BSβ}$-F79A, $P450_{BSβ}$-F173A, $P450_{BSβ}$-F289A or $P450_{BSβ}$-F292A), 0.5–10 mM substrate (**1**–**7**), 5 μM AldO, and 5% EtOH as co-solvent. The reactions were performed at 30 °C for 6 h, 12 h, or 24 h in a final volume of 200 μL.

### Steady-state kinetic analysis

Determination of the steady-state kinetic parameters was carried out as follows: 0.02–1 μM P450 enzyme ($P450_{BSβ}$ or $P450_{BSβ}$-F46A), 5 μM AldO, and varying substrate concentrations (0.1–8 mM) in a 1 mL reaction system (pH 7.4, 50 mM $NaH_2PO_4$, 10% glycerol). The synthesis of *d*-fluchloraminopyr (*d*-**7**) is described in Supplementary Method 4. The reaction was initiated by adding P450 enzyme at 30 °C. Aliquots (200 μL) of reactions were removed and quenched at fixed time points (0, 10, 20, 30, and 60 min) by adding 200 μL methanol for reaction termination. Proteins were removed by centrifugation at 14,000 × *g* for 10 min. The supernatants were subjected to HPLC analysis to monitor substrate consumption by each enzyme within the linear range, enabling calculation of the initial rates. All measurements were conducted in triplicate, and the rates determined at various substrate concentrations were fitted to the Michaelis–Menten equation to calculate the steady-state kinetic parameters using OriginPro 8.5 program.

### Determination of substrate dissociation constants

The 1 mL reaction mixture containing 1 μM of P450 ($P450_{BSβ}$, $P450_{BSβ}$-F46A, or $P450_{BSβ}$-F46A-R242A) in the corresponding reaction buffer was titrated with sequential additions of 1–10 mM substrate stock (**1**–**7**) dissolved in 10% ethanol (1–20 μL). The amount of ethanol cannot exceed 1% *vol*/*vol*. The difference spectra were recorded at room temperature on a Molecular Devices Spectra Max M2 spectrometer in the wavelength range of 350–500 nm. The absorbance changes at 390 nm and 420 nm ($\Delta A = A_{390} - A_{420}$) were fitted as a function of substrate concentrations ($\Delta A = A_{max}[S]/(K_D + [S])$) using OriginPro 8.5 program to calculate the dissociation constants ($K_D$)[81,82], where $A_{max}$ is the maximum absorbance shift at saturation, [*S*] is the total substrate concentration.

**Time-course experiments.** The reaction mixture contained a certain reaction buffer, 1 μM P450, 0.5 mM substrate (**3**, **6**, **7**, **8** or **12**) in a 1.2 mL reaction system. The reaction was initiated by adding 5 μM AldO at 30 °C. Aliquots (200 μL) of the reactions were taken and quenched at different time points (0, 1, 5, 30, and 120 min) by adding 200 μL methanol. Sample extraction and analysis were performed by following the HPLC analytical method described in Supplementary Method 1.

**Detection of glyoxylic acid/pyruvic acid/4-oxobutanoic acid.** The detection of glyoxylic acid, pyruvic acid, or 4-oxobutanoic acid was performed using a classical method based on 2,4-dinitrophenylhydrazine (DNPH) derivatization under aqueous acidic conditions[83,84], and the coupling product was monitored by LC-MS. In order to avoid the adverse effect of glyceraldehyde in AldO-glycerol system, 1 mM exogenous $H_2O_2$ was added. The reaction containing 1 μM $P450_{BSβ}$, $P450_{BSβ}$-F46A, or $P450_{BSβ}$-F173A, 500 μM substrate (**1**–**7**), 1 mM $H_2O_2$, 5% EtOH as co-solvent in 200 μL reaction buffer (pH 7.4, 50 mM $NaH_2PO_4$, 10% glycerol) was carried out at 30 °C for 6 h. The reaction was quenched by adding 20 μL 1 M HCl and extracted with an equal volume of chloroform, and 150 μL aqueous phase was mixed with

1 mM DNPH (excess) and incubated at 50 °C for 1 h. After derivatization, ethyl acetate was used for extraction and then dried by nitrogen blow. Later, 100 µL of the sample in acetonitrile was used for HPLC and LC-MS analysis.

### Molecular docking

The initial structures of **1**–**3**, **5**, and **7** were optimized through density functional theory (DFT). Automated molecular docking was performed using the DFT-optimized structures with the AutoDock Vina program (version 1.5.6) integrated with AutoDockTools (ADT)[85]. Receptor-ligand complexes preparation followed the guidelines provided in AutoDock manual, with polar hydrogens added using AutoDockTools. The docking grid box was centered on the substrate-binding pocket adjacent to the heme Fe–$H_2O_2$ moiety. The grid center coordinates were $x = 29.2$, $y = 27.8$, and $z = 42.3$ Å. The grid box dimensions were set to 20.0 × 20.0 × 20.0 Å, which covered the ligand-binding pocket, the distal heme region, and the surrounding catalytic residues. The exhaustiveness parameter was set to 32, with num_modes = 20 and energy_range = 4 kcal $mol^{-1}$. All side chains remained fixed during docking calculations while a suitable grid enclosing heme's active site was defined through the model visualization in AutoDockTools. Default parameter settings along with top-scoring docked conformations served as input for subsequent analyses in this study. Visualization and analysis of resulting docked models employed ADT alongside PyMOL version 2.3.2 (https://pymol.org/2/).

### MD, QM/MM, and QM calculations

**MD.** The Amber ff14SB[86] force field was selected for treating the amino acid residues of the $P450_{BS\beta}$-F46A protein (PDB accession code: 9IY1)[87], while the AMBER force field (GAFF)[88] was employed for the substrate. Besides, the RESP calculations[89] at the HF/6-31 G* level of theory were used to define the partial atomic charges of the substrate. The parmchk utility in AmberTools 18 was used to load the missing parameters of the substrate. Then, six $Na^+$ counterions were added to neutralize the total charge of the complex system, and no additional NaCl was added. Finally, the whole system was solvated in a rectangular box with TIP3P waters (~23,300 water molecules), with a minimum distance of 15 Å from the protein surface. After the setup of the system, it was totally minimized by the combined steepest descent and conjugate gradient methods. The system was gently annealed from 10 to 300 K under the canonical ensemble for 50 ps with a small restraint of 15 kcal/mol/Å on the protein. In order to get a uniform density, 1 ns of density equilibration was then performed under the NPT ensemble at the target temperature of 300 K and the pressure of 1.0 atm. The temperature was controlled using a Langevin thermostat with a collision frequency of 2.0 $ps^{-1}$. Long-range electrostatic interactions were treated using the particle mesh Ewald method, and a nonbonded cutoff of 8.0 Å was applied for real-space interactions. The pressure was maintained at 1.0 atm using the Berendsen barostat with isotropic pressure coupling and a pressure relaxation time of 2.0 ps. Afterwards, we removed all the restraints on the protein and further equilibrated the system for 10 ns under the NPT ensemble to get a stable temperature and pressure. At last, we performed a productive MD simulation under the NPT ensemble for 200 ns. During the MD, the covalent bonds containing hydrogen were constrained using SHAKE, and an integration step of 2 fs was used. All the MD processes were conducted using the Amber 18 package. The OriginPro Learning Edition (https://www.originlab.com/OriginProLearning.aspx) was used for the visualization of the MD and QM data.

**QM/MM.** For the subsequent QM/MM calculations, we selected the representative snapshot from each classical MD trajectory. All the QM/MM calculations were performed by the ChemShell[90], in which the turbomole[91] is invoked for the QM region while the DL_POLY[92] is used for the MM region. Besides, the electronic embedding scheme[93] was employed to account for the polarizing effect of the enzyme environment on the QM region, while the hydrogen link atoms with the charge-shift model were used to deal with the QM/MM boundary. Here, the QM region was studied with the hybrid B3LYP[94,95] density functional, which has been proven to be reliable for the simulation of the P450 complex systems[96–98]. In this study, the double-ζ basis set def2-SVP (B1) was used for geometry optimization, while the energies were corrected with the larger basis set def2-TZVP (B2) for all the QM region atoms. The dispersion corrections with Grimme's D3 method[99] were added in all QM calculations. Similar to QM calculations, the QM region included the substrate, either the HEM–Fe(IV) = $O^{2-}$ species or the HEM–Fe(III)···$H_2O_2$ complex of $P450_{BS\beta}$-F46A, the Fe-coordinated sulfur atom of Cys363, and the side chain of Arg242 (see Fig. 4). For the heme cofactor, all peripheral substituents attached to the porphyrin macrocycle were truncated, while the porphyrin plane, the Fe center, and the axial/reactive oxygen ligand were retained in the QM region. For Arg242, the QM/MM boundary was placed at the Cα–Cβ bond connecting the side chain to the protein backbone. For Cys363, only the Fe-coordinated sulfur atom was retained in the QM region, and the QM/MM boundary was placed at the Sγ–Cβ bond. All dangling valences generated by these truncations were saturated with hydrogen link atoms, which were placed along the original covalent bond directions. No link atom was introduced on the Fe–O bond, Fe–S coordination bond, or any bond directly involved in the chemical reaction. All the transition states (TSs) were located by relaxed potential energy surface (PES) scans followed by full TS optimizations using the DL-FIND code[100]. The QM/MM energy is provided in Source Data file.

**QM.** For the non-enzymatic reaction, the intermediate species with a hydrated cluster model[101,102] were optimized in conjunction with the SMD continuum solvation model at the BMK/6–31 G(d) level of theory. All QM model calculations were performed with the Gaussian 16 software. The energies were further refined with the larger basis set 6–311 + + G(d,p) for all atoms. The dispersion energies were included in both optimizations and single-point energy calculations. The QM energy is shown in Supplementary Table 16.

**Umbrella sampling.** The dynamic and thermodynamic features governing the entry of substrate **7** and intermediate **8** from the solvent into the active site of wild-type $P450_{BS\beta}$ and $P450_{BS\beta}$-F46A were characterized using umbrella sampling in combination with the weighted histogram analysis method (WHAM)[103]. Initial configurations were extracted from equilibrated states obtained in MD simulations, and the reaction coordinate was defined as the distance between the heme Fe atom and the center of mass of the substrate. Umbrella sampling windows were generated along the reaction coordinate at intervals of 0.2 Å. For each window, 10 ns of MD simulations were conducted under a harmonic biasing potential with a force constant of 50 kcal $mol^{-1}$ $Å^{-2}$. The unbiased potentials of mean force were subsequently reconstructed using WHAM, providing quantitative free-energy profiles for substrate translocation from the external environment into the enzyme active site.

### Plant experiments

**Construction of the transgenic plants.** The coding sequence of $P450_{BS\beta}$-F46A-CPR was codon optimized for its expression in rice. A chloroplast-localization signal (CLS) of 47 amino acid residues derived from *Oryza sativa L.* (sequence: MAPTVMASSATSVAPFQGLKSTA GLPVSRRSNSAGLGSVSNGGRISC)[60] was fused to the *N*-terminus of the codon-optimized $P450_{BS\beta}$-F46A-CPR. A 3×Flag-tag was inserted between the CLS and the codon-optimized *$P450_{BS\beta}$-F46A-CPR*. Besides, the gene blocks include either the CLS, Flag-tag and $P450_{BS\beta}$-F46A-CPR or the CLS, Flag-tag, $P450_{BS\beta}$-F46A-CPR and GFP, and were synthesized and then cloned into the pCambia1301 vector. The UBI promoter was

used to drive the expression of $P450_{BS\beta}$-F46A-CPR. These plasmids were then prepared for transfection into rice protoplast cells.

**Rice protoplast transformation**. Protoplast cells were prepared and transformed as previously described[104]. In brief, the sterilized rice seeds were sterilized, germinated, and grown in a chamber for 12–17 days. Green tissues from the stems and sheathes of rice seedlings were used to prepare protoplast cells using the cell wall-dissolving enzyme solution. PEG 4000 (polyethene glycol 4000)-mediated transfections were then performed on the isolated protoplasts.

**Rice transformation.** Rice callus was prepared and transformed according to a previously established method[104]. Briefly, calli were induced from mature embryos of the elite *japonica* rice variety Jingeng 818[56], followed by Agrobacterium-mediated transformation. Subsequently, the transformed calli were cultivated and subjected to hygromycin selection. Surviving calli were then moved to differentiation media to promote shoot and root formation to generate T0 plantlets. The plantlets were transplanted into plant culture pots in a greenhouse after 7 days of acclimatization in a plant growth chamber. Positive events were screened through PCR using target-specific primers and Sanger sequencing verification of the amplicons.

### Protein expression verification by western blotting and subcellular localization

**Protein expression verification by western blotting.** The leaf tissue of transgenic rice was finely powdered in liquid nitrogen. Proteins were homogenized in 2 × SDS buffer and then centrifuged to remove undissolved debris. The supernatant containing dissolved proteins was then separated on SDS-PAGE and transferred onto a PVDF membrane by the semidry blotting method. Western blotting was conducted using Sigma monoclonal anti-Flag M2-Peroxidase antibody (Sigma-Aldrich, A8592, dilution 1:1000), with detection facilitated by the Amersham ECL Prime reagent. Actin was used as an internal control, and the corresponding anti-actin was provided by Sangon Biotech.

**Protein expression verification by subcellular localization.** In the rice protoplast system, protein $P450_{BS\beta}$-F46A-CPR is expressed as a green fluorescent protein (GFP) fusion protein (excitation at 488 nm and emission at 509 nm) to facilitate subcellular localization studies. Confocal microscopy was performed using the LSM880 laser scanning confocal microscope (Zeiss), and the fluorescent confocal images of the plant protoplasts were exported using ZEN software, version 2.0 (black edition, Zeiss).

### Herbicide susceptibility tests for transgenic rice

**Growth inhibition assay of plants on plates.** Transgenic rice expressing *$P450_{BS\beta}$-F46A-CPR* was selected with hygromycin. Herbicide susceptibility was evaluated using seeds of T1 transgenic and nontransgenic (control, *japonica* rice variety Jingeng 818) rice plants on solid MS medium containing **19** (0.03 μM), which were cultured at 25 °C for 21 days.

**Plant growth inhibition assay by spraying.** The control experiments were treated solely with a solvent containing DMSO. The spraying treatments commenced when the T1 seedlings reached the three-leaf stage. For **19**, the field application rate was 40/80 grams of active ingredient per hectare (g.a.i. $ha^{-1}$), applied once at 25 °C for a duration of 22 days.

### Reporting summary

Further information on research design is available in the Nature Portfolio Reporting Summary linked to this article.

## Data availability

Previously published structures used in this study include PDB ID codes: 2P1N (the crystal structure of **1**-bound TIR1, https://doi.org/10.2210/pdb2P1N/pdb), 5BKB (the crystal structure of **2**-bound RdpA, https://doi.org/10.2210/pdb5BKB/pdb), 6E1Q (the crystal structure of **3**-bound AtGH3.15, https://doi.org/10.2210/pdb6E1Q/pdb), 1IZO (the crystal structure of palmitic acid-bound $P450_{BS\beta}$, https://doi.org/10.2210/pdb1IZO/pdb), and 9IY1 (the crystal structure of $P450_{BS\beta}$-F46A, https://doi.org/10.2210/pdb9IY1/pdb). All other relevant data supporting the findings of this study are available in this manuscript and Supplementary Information. Source data are provided with this paper.

## References


1. Yan, Y. et al. Resistance-gene-directed discovery of a natural-product herbicide with a new mode of action. *Nature* **559**, 415–418 (2018).
2. Rey-Caballero, J. et al. Unravelling the resistance mechanisms to 2,4-D (2,4-dichlorophenoxyacetic acid) in corn poppy (*Papaver rhoeas*). *Pestic. Biochem. Physiol.* **133**, 67–72 (2016).
3. Gaines, T. A. et al. Mechanisms of evolved herbicide resistance. *J. Biol. Chem.* **295**, 10307–10330 (2020).
4. Powles, S. B. & Yu, Q. Evolution in action: plants resistant to herbicides. *Annu. Rev. Plant Biol.* **61**, 317–347 (2010).
5. Woodward, A. W. & Bartel, B. Auxin: regulation, action, and interaction. *Ann. Bot.* **95**, 707–735 (2005).
6. Sherp, A. M., Lee, S. G., Schraft, E. & Jez, J. M. Modification of auxinic phenoxyalkanoic acid herbicides by the acyl acid amido synthetase GH3.15 from *Arabidopsis*. *J. Biol. Chem.* **293**, 17731–17738 (2018).
7. Grossmann, K. Auxin herbicides: current status of mechanism and mode of action. *Pest Manag. Sci.* **66**, 113–120 (2010).
8. Todd, O. E. et al. Synthetic auxin herbicides: finding the lock and key to weed resistance. *Plant Sci.* **300**, 110631 (2020).
9. Zhou, W. et al. Degradation of a novel herbicide fluchloraminopyr in soil: dissipation kinetics, degradation pathways, transformation products identification and ecotoxicity assessment. *Environ. Int.* **193**, 109135 (2024).
10. Nandula, V. K. Herbicide resistance traits in maize and soybean: current status and future outlook. *Plants* **8**, 337 (2019).
11. Hussain, A. et al. Herbicide resistance: another hot agronomic trait for plant genome editing. *Plants* **10**, 621 (2021).
12. Behrens, M. R. et al. Dicamba resistance: enlarging and preserving biotechnology-based weed management strategies. *Science* **316**, 1185–1188 (2007).
13. Gould, F., Brown, Z. S. & Kuzma, J. Wicked evolution: Can we address the sociobiological dilemma of pesticide resistance?. *Science* **360**, 728–732 (2018).
14. Lyu, J. Novel gene for herbicide resistance. *Nat. Plants* **9**, 1576–1576 (2023).
15. Watkinson, A. R., Freckleton, R. P., Robinson, R. A. & Sutherland, W. J. Predictions of biodiversity response to genetically modified herbicide-tolerant crops. *Science* **289**, 1554–1557 (2000).
16. Green, J. M. The benefits of herbicide-resistant crops. *Pest Manag. Sci.* **68**, 1323–1331 (2012).
17. Dharmasiri, N., Dharmasiri, S. & Estelle, M. The F-box protein TIR1 is an auxin receptor. *Nature* **435**, 441–445 (2005).
18. Kepinski, S. & Leyser, O. The *Arabidopsis* F-box protein TIR1 is an auxin receptor. *Nature* **435**, 446–451 (2005).
19. Castle, L. A. et al. Discovery and directed evolution of a glyphosate tolerance gene. *Science* **304**, 1151–1154 (2004).
20. Serbent, M. P., Rebelo, A. M., Pinheiro, A., Giongo, A. & Tavares, L. B. B. Biological agents for 2,4-dichlorophenoxyacetic acid herbicide degradation. *Appl. Microbiol. Biotechnol.* **103**, 5065–5078 (2019).

21. Chekan, J. R. et al. Molecular basis for enantioselective herbicide degradation imparted by aryloxyalkanoate dioxygenases in transgenic plants. *Proc. Natl. Acad. Sci. USA* **116**, 13299–13304 (2019).
22. Wright, T. R. et al. Robust crop resistance to broadleaf and grass herbicides provided by aryloxyalkanoate dioxygenase transgenes. *Proc. Natl. Acad. Sci. USA* **107**, 20240–20245 (2010).
23. Müller, T. A., Fleischmann, T., van der Meer, J. R. & Kohler, H. P. Purification and characterization of two enantioselective α-ketoglutarate-dependent dioxygenases, RdpA and SdpA, from *Sphingomonas herbicidovorans* MH. *Appl. Environ. Microbiol.* **72**, 4853–4861 (2006).
24. Tan, X. et al. Mechanism of auxin perception by the TIR1 ubiquitin ligase. *Nature* **446**, 640–645 (2007).
25. Siminszky, B. Plant cytochrome P450-mediated herbicide metabolism. *Phytochem. Rev.* **5**, 445–458 (2006).
26. Dimaano, N. G. & Iwakami, S. Cytochrome P450-mediated herbicide metabolism in plants: current understanding and prospects. *Pest Manag. Sci.* **77**, 22–32 (2021).
27. Schuler, M. A. & Werck-Reichhart, D. Functional genomics of P450s. *Annu. Rev. Plant Biol.* **54**, 629–667 (2003).
28. Liu, Y. et al. Hydrogen peroxide-independent production of α-alkenes by $OleT_{JE}$ P450 fatty acid decarboxylase. *Biotechnol. Biofuels* **7**, 28 (2014).
29. Li, Z. et al. Engineering cytochrome P450 enzyme systems for biomedical and biotechnological applications. *J. Biol. Chem.* **295**, 833–849 (2020).
30. Guengerich, F. P. Common and uncommon cytochrome P450 reactions related to metabolism and chemical toxicity. *Chem. Res. Toxicol.* **14**, 611–650 (2001).
31. Meunier, B., de Visser, S. P. & Shaik, S. Mechanism of oxidation reactions catalyzed by cytochrome P450 enzymes. *Chem. Rev.* **104**, 3947–3980 (2004).
32. Coon, M. J. Cytochrome P450: nature's most versatile biological catalyst. *Annu. Rev. Pharmacol. Toxicol.* **45**, 1–25 (2005).
33. Rittle, J. & Green, M. T. Cytochrome P450 compound I: capture, characterization, and C-H bond activation kinetics. *Science* **330**, 933–937 (2010).
34. Yosca, T. H. et al. Iron(IV)hydroxide pK(a) and the role of thiolate ligation in C-H bond activation by cytochrome P450. *Science* **342**, 825–829 (2013).
35. Chen, K. & Arnold, F. H. Engineering new catalytic activities in enzymes. *Nat. Catal.* **3**, 203–213 (2020).
36. Reetz, M. T., Qu, G. & Sun, Z. Engineered enzymes for the synthesis of pharmaceuticals and other high-value products. *Nat. Synth.* **3**, 19–32 (2024).
37. Lee, D. S. et al. Substrate recognition and molecular mechanism of fatty acid hydroxylation by cytochrome P450 from *Bacillus subtilis*. Crystallographic, spectroscopic, and mutational studies. *J. Biol. Chem.* **278**, 9761–9767 (2003).
38. Fujishiro, T. et al. Crystal structure of $H_2O_2$-dependent cytochrome $P450_{SP\alpha}$ with its bound fatty acid substrate: insight into the regioselective hydroxylation of fatty acids at the α position. *J. Biol. Chem.* **286**, 29941–29950 (2011).
39. Belcher, J. et al. Structure and biochemical properties of the alkene producing cytochrome P450 $OleT_{JE}$ (CYP152L1) from the *Jeotgalicoccus* sp. 8456 bacterium. *J. Biol. Chem.* **289**, 6535–6550 (2014).
40. Munro, A. W., McLean, K. J., Grant, J. L. & Makris, T. M. Structure and function of the cytochrome P450 peroxygenase enzymes. *Biochem. Soc. Trans.* **46**, 183–196 (2018).
41. Jiang, Y. & Li, S. P450 fatty acid decarboxylase. *Methods Enzymol.* **693**, 339–374 (2023).
42. Sigmund, M. C. & Poelarends, G. J. Current state and future perspectives of engineered and artificial peroxygenases for the oxyfunctionalization of organic molecules. *Nat. Catal.* **3**, 690–702 (2020).
43. Jiang, Y., Li, P., Li, Z., Zhang, B. & Li, S. Photoenzymatic synthesis of 1-alkenes and hydroxyl fatty acids by cascading a COF photocatalyst and P450 peroxygenases. *Sci. Bull.* **69**, 3350–3354 (2024).
44. Li, Z., Jiang, Y., Li, N. & Li, S. Efficient and enantioselective biosynthesis of (*R*)-mandelic acid derivatives using CYP152 peroxygenases. *Sci. Bull.* **71**, 1287–1292 (2026).
45. Jiang, Y. et al. Unexpected reactions of α,β-unsaturated fatty acids provide insight into the mechanisms of CYP152 peroxygenases. *Angew. Chem. Int. Ed.* **60**, 24694–24701 (2021).
46. Wang, S., Jiang, S., Chen, H., Bai, W. & Wang, X. Directed evolution of a hydroxylase into a decarboxylase for synthesis of 1-alkenes from fatty acids. *ACS Catal.* **10**, 14375–14379 (2020).
47. Weiss, G. A., Watanabe, C. K., Zhong, A., Goddard, A. & Sidhu, S. S. Rapid mapping of protein functional epitopes by combinatorial alanine scanning. *Proc. Natl. Acad. Sci. USA* **97**, 8950–8954 (2000).
48. Morrison, K. L. & Weiss, G. A. Combinatorial alanine-scanning. *Curr. Opin. Chem. Biol.* **5**, 302–307 (2001).
49. Cheng, M., Chen, D., Parales, R. E. & Jiang, J. Oxygenases as powerful weapons in the microbial degradation of pesticides. *Annu. Rev. Microbiol.* **76**, 325–348 (2022).
50. Jiang, Y. et al. Unexpected activities of CYP152 peroxygenases towards non-carboxylic substrates reveal novel substrate recognition mechanism and catalytic versatility. *Angew. Chem. Int. Ed.* **137**, e202506614 (2025).
51. Shaik, S., Kumar, D., de Visser, S. P., Altun, A. & Thiel, W. Theoretical perspective on the structure and mechanism of cytochrome P450 enzymes. *Chem. Rev.* **105**, 2279–2328 (2005).
52. Chen, Z. & Yin, G. The reactivity of the active metal oxo and hydroxo intermediates and their implications in oxidations. *Chem. Soc. Rev.* **44**, 1083–1100 (2015).
53. Rendina, A. R. et al. Kinetic characterization, stereoselectivity, and species selectivity of the inhibition of plant acetyl-CoA carboxylase by the aryloxyphenoxypropionic acid grass herbicides. *Arch. Biochem. Biophys.* **265**, 219–225 (1988).
54. Zhou, J. et al. Recent insights into the microbial catabolism of aryloxyphenoxy-propionate herbicides: Microbial resources, metabolic pathways and catabolic enzymes. *World J. Microb. Biot.* **34**, 117 (2018).
55. Dill, G. M. Glyphosate-resistant crops: history, status and future. *Pest Manag. Sci.* **61**, 219–224 (2005).
56. Lu, Y. et al. A donor-DNA-free CRISPR/Cas-based approach to gene knock-up in rice. *Nat. Plants* **7**, 1445–1452 (2021).
57. Munro, A. W. et al. P450 BM3: the very model of a modern flavocytochrome. *Trends Biochem. Sci.* **27**, 250–257 (2002).
58. Lu, C. et al. An engineered self-sufficient biocatalyst enables scalable production of linear α-olefins from carboxylic acids. *ACS Catal.* **8**, 5794–5798 (2018).
59. Wise, C. E., Hsieh, C. H., Poplin, N. L. & Makris, T. M. Dioxygen activation by the biofuel-generating cytochrome P450 OleT. *ACS Catal.* **8**, 9342–9352 (2018).
60. Park, S., Jeong, J. S., Do Choi, Y. & Kim, J. Characterization of the rice RbcS3 promoter and its transit peptide for use in chloroplast-targeted expression. *Plant Biotechnol. Rep.* **9**, 395–403 (2015).
61. Vain, P., Worland, B., Kohli, A., Snape, J. & Christou, P. The green fluorescent protein (GFP) as a vital screenable marker in rice transformation. *Theor. Appl. Genet.* **96**, 164–169 (1998).
62. Krähmer, H. et al. What makes a molecule a pre- or a post-herbicide–how valuable are physicochemical parameters for their design? *Pest Manag. Sci.* **77**, 4863–4873 (2021).
63. LeClere, S., Wu, C., Westra, P. & Sammons, R. D. Cross-resistance to dicamba, 2,4-D, and fluroxypyr in *Kochia scoparia* is endowed

by a mutation in an AUX/IAA gene. *Proc. Natl. Acad. Sci. USA* **115**, E2911–E2920 (2018).
64. Kumar, A., Trefault, N. & Olaniran, A. O. Microbial degradation of 2,4-dichlorophenoxyacetic acid: Insight into the enzymes and catabolic genes involved, their regulation and biotechnological implications. *Crit. Rev. Microbiol.* **42**, 194–208 (2016).
65. Ren, H., Li, Q., Zhan, Y., Fang, X. & Yu, D. 2, 4-Dichlorophenol hydroxylase for chlorophenol removal: Substrate specificity and catalytic activity. *Enzym. Microb. Tech.* **82**, 74–81 (2016).
66. Werck-Reichhart, D., Hehn, A. & Didierjean, L. Cytochromes P450 for engineering herbicide tolerance. *Trends Plant Sci.* **5**, 116–123 (2000).
67. Zhang, K. et al. Biocatalytic enantioselective $\beta$-hydroxylation of unactivated C–H bonds in aliphatic carboxylic acids. *Angew. Chem. Int. Ed.* **61**, e202204290 (2022).
68. Ariyasu, S., Stanfield, J. K., Aiba, Y. & Shoji, O. Expanding the applicability of cytochrome P450s and other haemoproteins. *Curr. Opin. Chem. Biol.* **59**, 155–163 (2020).
69. Hayashi, K. et al. The main oxidative inactivation pathway of the plant hormone auxin. *Nat. Commun.* **12**, 6752 (2021).
70. Bartel, B. Auxin biosynthesis. *Annu. Rev. Plant Biol.* **48**, 51–66 (1997).
71. Fuchs, G., Boll, M. & Heider, J. Microbial degradation of aromatic compounds—from one strategy to four. *Nat. Rev. Microbiol.* **9**, 803–816 (2011).
72. Gumulya, Y. et al. Engineering highly functional thermostable proteins using ancestral sequence reconstruction. *Nat. Catal.* **1**, 878–888 (2018).
73. Hansen, C. C., Nelson, D. R., Møller, B. L. & Werck-Reichhart, D. Plant cytochrome P450 plasticity and evolution. *Mol. Plant* **14**, 1244–1265 (2021).
74. Leveson-Gower, R. B., Mayer, C. & Roelfes, G. The importance of catalytic promiscuity for enzyme design and evolution. *Nat. Rev. Chem.* **3**, 687–705 (2019).
75. Zhao, K. & Rhee, S. Y. Omics-guided metabolic pathway discovery in plants: resources, approaches, and opportunities. *Curr. Opin. Plant Biol.* **67**, 102222 (2022).
76. Yuan, J., Li, Q., Li, X. & Su, C. AI-based protein engineering: a novel strategy for enhancing broad-spectrum plant resistance. *Mol. Plant* **17**, 1648–1650 (2024).
77. Xu, H. et al. In vitro oxidative decarboxylation of free fatty acids to terminal alkenes by two new P450 peroxygenases. *Biotechnol. Biofuels* **10**, 208 (2017).
78. Omura, T. & Sato, R. The carbon monoxide-binding pigment of liver microsomes. I. Evidence for its hemoprotein nature. *J. Biol. Chem.* **239**, 2370–2378 (1964).
79. Heuts, D. P., van Hellemond, E. W., Janssen, D. B. & Fraaije, M. W. Discovery, characterization, and kinetic analysis of an alditol oxidase from *Streptomyces coelicolor*. *J. Biol. Chem.* **282**, 20283–20291 (2007).
80. Jiang, Y. et al. Biochemical characterization of three new α-olefin-producing P450 fatty acid decarboxylases with a halophilic property. *Biotechnol. Biofuels* **12**, 79 (2019).
81. Isin, E. M. & Guengerich, F. P. Kinetics and thermodynamics of ligand binding by cytochrome P450 3A4. *J. Biol. Chem.* **281**, 9127–9136 (2006).
82. Isin, E. M. & Guengerich, F. P. Substrate binding to cytochromes P450. *Anal. Bioanal. Chem.* **392**, 1019–1030 (2008).
83. Mao, Y., Wang, X., Tang, S., Yang, H. & Xie, Y. Determination of ketoacids in drinking water by DNPH derivatization and LC-ESI-MS/MS. *Anal. Methods* **7**, 6207–6212 (2015).
84. El-Maghrabey, M., Suzuki, H., Kishikawa, N. & Kuroda, N. A sensitive chemiluminescence detection approach for determination of 2,4-dinitrophenylhydrazine derivatized aldehydes using online UV irradiation-luminol CL reaction. Application to the HPLC analysis of aldehydes in oil samples. *Talanta* **233**, 122522 (2021).
85. Morris, G. M. et al. AutoDock4 and AutoDockTools4: automated docking with selective receptor flexibility. *J. Comput. Chem.* **30**, 2785–2791 (2009).
86. Maier, J. A. et al. ff14SB: Improving the accuracy of protein side chain and backbone parameters from ff99SB. *J. Chem. Theory Comput.* **11**, 3696–3713 (2015).
87. Shoji, O. et al. Understanding substrate misrecognition of hydrogen peroxide dependent cytochrome P450 from *Bacillus subtilis*. *J. Biol. Inorg. Chem.* **15**, 1331–1339 (2010).
88. Wang, J., Wolf, R. M., Caldwell, J. W., Kollman, P. A. & Case, D. A. Development and testing of a general amber force field. *J. Comput. Chem.* **25**, 1157–1174 (2004).
89. Bayly, C. I., Cieplak, P., Cornell, W. & Kollman, P. A. A well-behaved electrostatic potential based method using charge restraints for deriving atomic charges: the RESP model. *J. Phys. Chem.* **97**, 10269–10280 (1993).
90. Metz, S., Kästner, J., Sokol, A. A., Keal, T. W. & Sherwood, P. ChemShell—a modular software package for QM/MM simulations. *WIRES Comput. Mol. Sci.* **4**, 101–110 (2013).
91. Furche, F. et al. Turbomole. *WIRES Comput. Mol. Sci.* **4**, 91–100 (2014).
92. Smith, W., Yong, C. & Rodger, P. DL_POLY: application to molecular simulation. *Mol. Simula.* **28**, 385–471 (2002).
93. Bakowies, D. & Thiel, W. Hybrid models for combined quantum mechanical and molecular mechanical approaches. *J. Phys. Chem.* **100**, 10580–10594 (1996).
94. Becke, A. D. Density-functional thermochemistry. II. The effect of the Perdew–Wang generalized-gradient correlation correction. *J. Chem. Phys.* **97**, 9173–9177 (1992).
95. Beeke, A. D. Density-functional thermochemistry. III. The role of exact exchange. *J. Chem. Phys.* **98**, 5648–5652 (1993).
96. Yagi, K., Yamada, K., Kobayashi, C. & Sugita, Y. Anharmonic vibrational analysis of biomolecules and solvated molecules using hybrid QM/MM computations. *J. Chem. Theory Comput.* **15**, 1924–1938 (2019).
97. Leth, R., Ercig, B., Olsen, L. & Jørgensen, F. S. Both reactivity and accessibility are important in cytochrome P450 metabolism: a combined DFT and MD study of fenamic acids in BM3 mutants. *J. Chem. Inf. Model.* **59**, 743–753 (2019).
98. Lonsdale, R. et al. Quantum mechanics/molecular mechanics modeling of regioselectivity of drug metabolism in cytochrome P450 2C9. *J. Am. Chem. Soc.* **135**, 8001–8015 (2013).
99. Grimme, S., Antony, J., Ehrlich, S. & Krieg, H. A consistent and accurate ab initio parametrization of density functional dispersion correction (DFT-D) for the 94 elements H-Pu. *J. Chem. Phys.* **132**, 154104 (2010).
100. Kästner, J. et al. DL-FIND: an open-source geometry optimizer for atomistic simulations. *J. Phys. Chem. A* **113**, 11856–11865 (2009).
101. Wang, B. & Cao, Z. Hydration of carbonyl groups: the labile H3O+ ion as an intermediate modulated by the surrounding water molecules. *Angew. Chem. Int. Ed.* **123**, 3324–3328 (2011).
102. Zhou, H. et al. Chemo-and regioselective dihydroxylation of benzene to hydroquinone enabled by engineered cytochrome P450 monooxygenase. *Angew. Chem. Int. Ed.* **131**, 774–778 (2019).
103. Kästner, J. Umbrella sampling. *WIREs Comput. Mol. Sci.* **1**, 932–942 (2011).
104. Shan, Q., Wang, Y., Li, J. & Gao, C. Genome editing in rice and wheat using the CRISPR/Cas system. *Nat. Protoc.* **9**, 2395–2410 (2014).

## Acknowledgements

We thank G.L., H.S., H.Y., X.Z., and S.W. from the State Key Laboratory of Microbial Technology, Shandong University for their assistance in collecting LC-MS and NMR data, as well as their support in laser scanning confocal microscopy imaging.

## Author contributions

Y.J., J.Z., S.M., W.P., and S.L. conceived this research. Y.J., J.Z., Zhong L., L.W., Y.G., Y.L., X.F., W.G., Y.L., Zijia L., J.D., G.Z., P.G., W.F., X.G., M.B., F.H., M.Z., H.H., B.W., S.M, H.L., W.P., and S.L. performed the experiments and analyzed the experimental results. Y.J., J.Z., S.M., W.P., and S.L. wrote the manuscript. All authors read and approved the manuscript.

## Funding

S.L. discloses support from the Key R&D Program of Shandong Province (No. 2025CXPT190), the National Key Research and Development Program of China (No. 2025YFA0923200), and the National Natural Science Foundation of China (No. 32025001). Y.J. discloses support from the National Natural Science Foundation of China (No. 32300021), Shandong Provincial Natural Science Foundation (Nos. ZR2023QC021, ZR2026MS0289), and Young Talent of Lifting Engineering for Science and Technology in Shandong (No. SDAST2026QTA090). Zhong.L. discloses support from the National Natural Science Foundation of China (No. 32200017), Shandong Provincial Natural Science Foundation (No. ZR2022QC070). W.P. discloses support from the National Natural Science Foundation of China (Nos. 22403094, 22577066), Shandong Provincial Natural Science Foundation (No. ZR2025QB36). B.W. discloses support from the National Natural Science Foundation of China (No. 22121001). J.Z., L.W., Y.G., Y.L., X.F., W.G., Y.L., Zijia.L., J.D., G.Z., P.G., W.F., X.G., M.B., F.H., M.Z., H.H., S.M., and H.L. declare no relevant funding.

## Competing interests

The authors declare no competing interests.

## Additional information

**Supplementary information** The online version contains supplementary material available at https://doi.org/10.1038/s41467-026-75811-1.

**Correspondence** and requests for materials should be addressed to Sudong Mo, Wei Peng or Shengying Li.

**Peer review information** *Nature Communications* thanks Kshatresh Dubey, and the other, anonymous, reviewer(s) for their contribution to the peer review of this work. A peer review file is available.